Reconciling volcanic deformation, degassing and petrological data using thermodynamic models

Stanley Tze Hou Yip[1,2], Juliet Biggs[1,2], Marie Edmonds[1,3], Philippa Liggins[3], Oliver Shorttle[3]

[1]Centre for the Observation and Modelling of Earthquakes, Volcanoes and Tectonics (COMET)
[2]School of Earth Sciences, University of Bristol, Wills Memorial Building, Bristol, BS8 1RJ, United Kingdom
[3]Department of Earth Sciences, University of Cambridge, Cambridge, CB2 3EQ, United Kingdom

Key Points:

- We use petrological data and a thermodynamic framework to model volcanic deformation and SO_2 degassing.
- High magmatic volatile content of arc basalts contributes to the lack of deformation observed at arc basalt eruptions.

Corresponding author: Stanley Tze Hou Yip, stanley.th.yip@bristol.ac.uk

Abstract

Two of the most widely observed co-eruptive volcanic phenomena - ground deformation and volcanic outgassing - are fundamentally linked via the mechanism of magma degassing and the development of compressibility, which controls how the volume of magma changes in response to a change in pressure. Here we use thermodynamic models (constrained by petrological data) to reconstruct volatile exsolution and the consequent changes in magma properties. Co-eruptive SO_2 degassing fluxes may be predicted from the mole fraction of exsolved SO_2 that develops in magma whilst stored prior to eruption and during decompression. Co-eruptive surface deformation may be predicted given estimates of erupted volume and the ratio between chamber compressibility and magma compressibility. We conduct sensitivity tests to assess how varying magma volatile content, crustal properties, and chamber geometry affect co-eruptive deformation and degassing. We find that magmatic H_2O content has the most impact on both SO_2 flux and volume change (normalised for erupted volumes). Our findings have general implications for typical arc and ocean island volcanic systems. The higher magmatic water content of arc basalts leads to a high pre-eruptive exsolved volatile content, making the magma more compressible than ocean island eruptions. Syn-eruptive gas fluxes are overall higher for arc eruptions, although SO_2 fluxes are similar for both settings (SO_2 flux for ocean island basalt eruptions is dominated by decompressional degassing). Our models are consistent with observation: deformation has been detected at 48% of ocean island eruptions (16/33) during the satellite era (2005-2020), but only 11% of arc basalt eruptions (7/61).

Plain Language Summary

Volcano monitoring provides a wealth of data upon which to base activity forecasts, yet we lack quantitative models to integrate two of the most widely observed eruptive parameters: ground deformation and volcanic gas fluxes. When magma exsolves volatiles (water, carbon dioxide, sulfur) during storage in the crust prior to eruptions, the fluid bubbles cause the magma to become compressible, and behave like a sponge. The effect of this degassing is that when pressure changes in the magma chamber (due to eruption, or due to recharge), the gas bubbles expand or contract in response, effectively maintaining a near-constant volume for the magma. Understanding the effect of magmatic gas on volume changes is key to developing integrated, satellite-based volcano monitoring approaches.

1 Introduction

The increasing number of satellite missions launched in the past decade has driven an explosion in data for studying the Earth's dynamic processes (Chaussard et al., 2013; Morales Rivera et al., 2016; Carn et al., 2017; Furtney et al., 2018; Biggs & Wright, 2020). The array of sensors onboard satellites routinely provides near real-time observations of volcanic eruptions such as SO_2 plumes and clouds (e.g., Carn et al., 2016; Carboni et al., 2016; Ge et al., 2016) and ground deformation (e.g., Biggs & Pritchard, 2017; Ebmeier et al., 2018; Pritchard et al., 2018), both of which are key indicators of eruption progress and may be used to track eruptive activity and understand pre-eruptive magma storage conditions. However, observations show that not all volcanoes exhibit pre- or co-eruptive deformation (Rivalta & Segall, 2008; Biggs et al., 2014; Reath et al., 2020); the causes of the wide variation in deformation systematics between volcanoes and between tectonic settings are not well understood (Piochi et al., 2005; Ebmeier et al., 2013b; Chaussard & Amelung, 2014). Reconciling observations of volcanic deformation and degassing can help identify the conditions that lead to the lack of observations of ground deformation (Kilbride et al., 2016; Reath et al., 2020). The magmatic processes that drive volcanic deformation and degassing are fundamentally linked: exsolution of volatiles from silicate melt in crustal magma reservoirs (during second boiling or due to decompression) causes magma to become compressible, fundamentally changing the volume-change response to pressure perturbations experienced by the magma during eruption and recharge (Woods & Huppert, 2003; Kilbride et al., 2016; Wong et al., 2017; Wong & Segall, 2020). However, while it is becoming increasingly common to compile multisensor data (e.g., Furtney et al., 2018; Reath et al., 2019, 2020), until recently there has not been a quantitative framework to jointly interpret observations of volcanic deformation and degassing, including CO_2 and SO_2 gas fluxes (Girona et al., 2014; Kilbride et al., 2016; Wong & Segall, 2020).

Thermodynamic models, constrained by petrological data, may be used to calculate the varying proportions of melt, crystals and exsolved volatiles in shallow magmatic reservoirs under a range of pressure, temperature and magma composition conditions (e.g., Papale et al., 2006; Gualda et al., 2012; Burgisser et al., 2015; Liggins et al., 2020, 2021). The exsolved volatile phase generated both during crystallisation and second boiling in the reservoir, and during decompressional degassing, contributes to the mass of gases released prior to and during an eruption (Wallace & Carmichael, 1992; Wallace,

2005). Since the physicochemical properties of magmas are interdependent, magma properties such as density and compressibility can be calculated using the law of conservation of mass (Spera, 2000; Huppert & Woods, 2002). The compressibility of magma and its surrounding host rock controls the co-eruptive volume change of magma chambers, which consequently affects co-eruptive ground deformation at the surface (e.g., Huppert & Woods, 2002; Edmonds et al., 2019; Head et al., 2019; Sigmundsson et al., 2020).

Previous work by Kilbride et al. (2016) introduced a thermodynamic framework for reconciling satellite observations of atmospheric sulfur yield and volcanic deformation during discrete explosive eruptions (where there is assumed to be little volatile exsolution during magma ascent). The framework uses thermodynamic models to illustrate the effect of initial magmatic volatile content (H_2O, CO_2) and oxygen fugacity on SO_2 degassing and volcanic deformation (Kilbride et al., 2016). Kilbride et al. (2016) then compared their model predictions to observations from 11 discrete explosive eruptions to illustrate the factors controlling volcanic deformation and degassing (Kilbride et al., 2016).

This study extends the thermodynamic framework developed by Kilbride et al. (2016) to enable large-scale analyses, such as sensitivity tests and Monte-Carlo simulations, across a wider range of magma compositions and eruption styles. The sensitivity tests for magma of basaltic composition explore how varying initial magmatic volatile contents (H_2O, CO_2, S) and oxygen fugacity affect magma properties and consequently volcanic deformation and degassing. We also consider the effects of variable crustal shear modulus μ and chamber geometry on co-eruptive volcanic deformation. Finally, we compare the properties of arc and ocean island magmas arising from their different volatile contents and discuss the implications for satellite observations of deformation and degassing during eruptions in different tectonic settings.

2 Background: Observations Of Volcanic Deformation and Degassing

Satellites with short repeat time and high spatial resolution provide consistent spatio-temporal coverage for monitoring volcanoes on regional to global scales (e.g., TerraSAR-X, Sentinel-1), which is particularly valuable for monitoring volcanoes with few or no ground-based stations (e.g., Telling et al., 2015; Carboni et al., 2016; Ebmeier et al., 2016; Delgado et al., 2017; Pritchard et al., 2018; Coppola et al., 2020). Interferometric Synthetic Aperture Radar (InSAR) is a satellite technique that measures the phase change

between pairs of satellite radar images to generate maps of surface displacement, which may be used to monitor volcanoes exhibiting deformation in response to changes in magma activity . However, while many volcanoes exhibit pre-eruptive inflation associated with magma intrusion and/or co-eruptive deflation during magma withdrawal, some do not (Moran et al., 2006; Rivalta & Segall, 2008; Biggs & Pritchard, 2017; Ebmeier et al., 2018). One of the possible reasons is due to the presence of an exsolved gas phase that is more compressible than the surrounding crust and silicate melt (Huppert & Woods, 2002; Woods & Huppert, 2003; Kilbride et al., 2016).

The most volumetrically significant volcanic volatile species produced during an eruption are H_2O and CO_2, yet it is difficult to distinguish these volatiles from atmospheric background in satellite measurements. In contrast, volcanic SO_2 has a strong absorption signal in the near-ultraviolet and infrared spectrum, and thus can be measured using satellite-based spectrometers (e.g., Carn et al., 2016; Carboni et al., 2016).

Conceptual models of magmatic systems may be used to understand different degassing configurations and their impact on monitoring signals (Figure 1). Volatiles are more soluble at higher pressures and hence they are largely dissolved in silicate melt in deep magmatic systems (Figure 1a). Volatiles exsolve during magma decompression, but if magma stalls in a chamber and cools, volatiles also exsolve during isobaric cooling and crystallisation, a process termed 'second boiling' (Edmonds et al., 2019).

For an explosive eruption, the high magma ascent rate limits volatile exsolution between the chamber and the surface (Figure 1b) and we make the simplifying assumption here that the gas emitted during the eruption is sourced entirely from the pre-eruptive exsolved volatile phase (Wallace & Gerlach, 1994; Wallace, 2005). In this case the amount of gases released (per unit of magma erupted) may be used to constrain the compressibility of the magma in the chamber prior to eruption, which will be related to the amount of deformation observed. In contrast, effusive eruptions involve a low magma ascent rate, such that volatiles exsolve extensively in the conduit (Figure 1c). In this case, the gases released during eruptions are mostly produced during magma ascent and cannot simply be related to the compressibility of the magma in the chamber prior to eruption without careful reconstruction of the degassing process using a thermodynamic model.

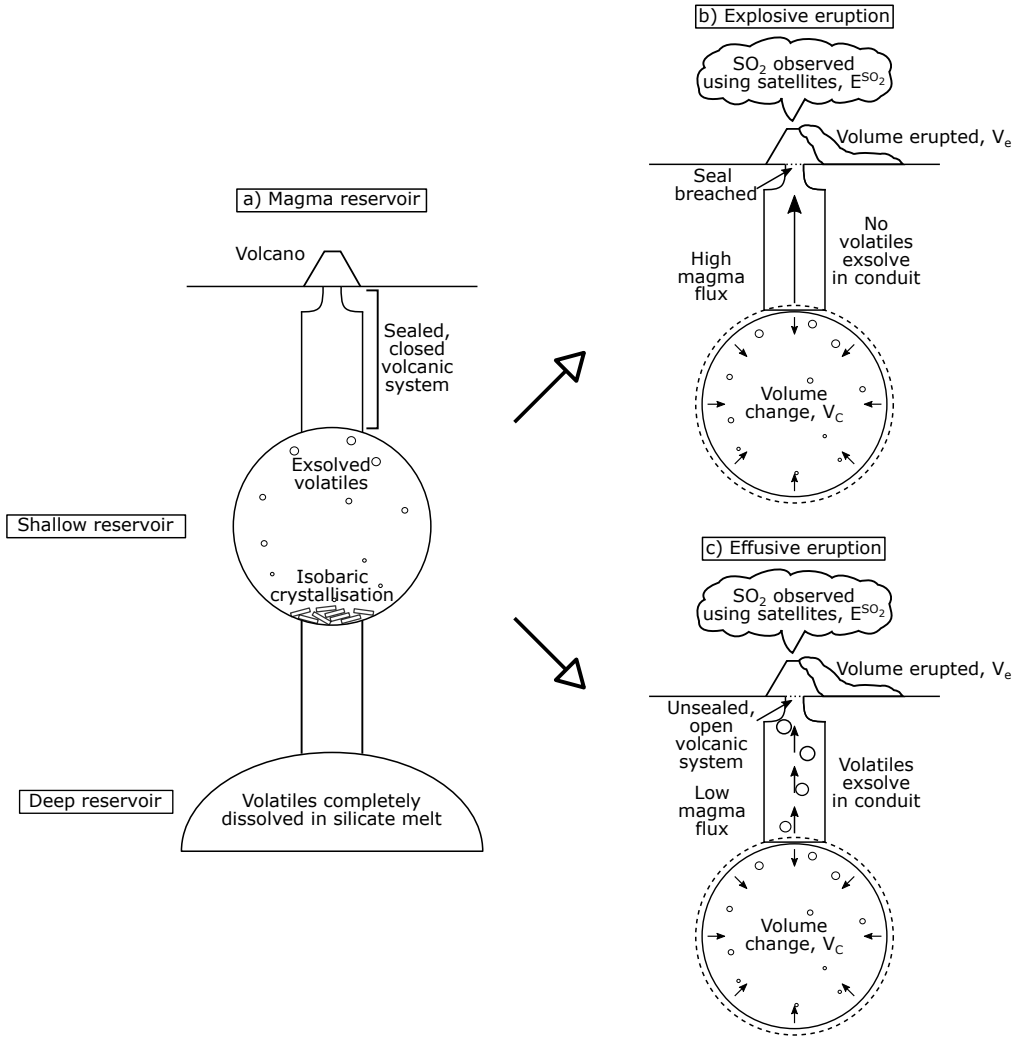

Figure 1. Conceptual model of magma degassing during eruptions of different styles. (a) Volcano with chambers at different depths, prior to an eruption. Magmatic volatiles are more soluble in deep magmatic chambers and thus a higher proportion of the total volatile load will be dissolved in the silicate melt. In the shallow chamber (at a lower pressure) there is a higher proportion of exsolved volatiles, with degassing being driven both by decompression as magma moves up from the lower chamber, and by crystallisation. (b) During explosive eruptions, magma is removed from the chamber and decompressed rapidly, with little volatile exsolution during magma ascent. Much of the volatiles emitted as gases during the eruption represents a pre-eruptive exsolved volatile phase that was present in the chamber prior to decompression (and which made the magma compressible). In this 'explosive' case we expect the volume change inferred from ground deformation at the surface to to be related to the amount of volatiles emitted during eruption (both normalised by erupted volume). (c) Effusive eruptions, on the other hand, are characterised by a low magma ascent rate between the chamber and the surface, allowing extensive volatile exsolution in the conduit, i.e., co-eruptive degassing. The volcanic gases observed at the surface are mostly derived from decompressional degassing and do not constrain the compressibility of the chamber. In this 'effusive' case, we do not expect a relationship between the amount of gases released during the eruption and the volume change inferred for the 'source' chamber during eruption.

3 Methodology

3.1 Thermodynamic modelling

Volatile solubility can be defined as the concentration of a volatile species that may be dissolved in magma at a particular set of pressure, temperature, melt composition and oxygen fugacity conditions (e.g., Scaillet & Pichavant, 2005; Duan, 2014; Burgisser et al., 2015). At equilibrium, the fugacity of each volatile species in the melt is equal to its fugacity in the fluid (Scaillet & Pichavant, 2005), such that a fraction of volatiles are dissolved in magma and the remainder are exsolved in the exsolved phase. Since magmatic volatiles are less soluble at low pressure, magma decompression is a principal driver for volatile exsolution (e.g., Papale, 1999; Duan, 2014; Burgisser et al., 2015).

Thermodynamic models based on mass balance and equilibrium constants may be used to calculate the mass and composition of the exsolved volatile phase and this may be then used to estimate bulk magma properties such as density and compressibility (Ohmoto & Kerrick, 1977; Gaillard & Scaillet, 2014). The concentration of each volatile species exsolved at any given pressure and temperature can be calculated using its corresponding solubility laws (e.g., Burgisser et al., 2015). Here, we use the Python implementation of EVo (Liggins et al., 2020, 2021) to predict the physicochemical properties of basaltic magma, such as the composition of the gas phase and magma density, as a function of melt composition, magmatic volatile content, oxygen fugacity of magma, temperature and pressure.

We use EVo to calculate magma and fluid compositions in the C-O-H-S-Fe system during magma decompression (Liggins et al., 2020, 2021). We initialise the model using the weight fraction of the volatile species H_2O, CO_2 and S as input parameters. The oxygen fugacity (f_{O_2}) is adjusted relative to the Ni-NiO buffer (NNO). EVo can be initialised by either 1) specifying starting pressure (p), and gas weight fraction (w_g), or 2) calculating the saturation pressure for the given composition (i.e., $w_g \approx 0$ wt%). Here we use the saturation point based on melt composition to find an appropriate starting pressure/depth (Liggins et al., 2021).

At a specified depth, the gas volume fraction (V_g) is controlled by the total gas weight fraction (w_g) and gas density (ρ_g):

$$V_g = (1 + \frac{MP(1 - w_g)}{RT\rho_M w_g})^{-1}, \quad (1)$$

where M is the average molar mass of the gas phase, R is the universal gas constant (8.3144 J/mol K) and ρ_M is the volatile-free magma density (Burgisser et al., 2015). Magma density (ρ_m) is a function of the density and volume fraction of both melt and gas (Spera, 2000):

$$\rho_m = \rho_g V_g + \rho_M (1 - V_g). \tag{2}$$

V_g increases during magma decompression and hence decreases ρ_m. Since ρ_m changes with p, magma compressibility (β_m) can be linked to the density and density gradient of magma with respect to pressure (Huppert & Woods, 2002):

$$\beta_m = \frac{1}{\rho_m} \frac{\delta \rho_m}{\delta p}. \tag{3}$$

Given how ρ_m changes with V_g, magma compressibility is dominated by the weight fraction of exsolved gas phase and hence magmatic volatile content (Kilbride et al., 2016; Edmonds et al., 2018).

Permeability develops when gas bubbles coalesce to form porous networks, thereby allowing exsolved volatiles to percolate through magma efficiently (Lowenstern, 1994; Candela, 1997; Bachmann & Bergantz, 2006; Collins et al., 2009; Lindoo et al., 2017). Magma becomes permeable when it reaches critical porosity, which is also defined as the percolation threshold (ϕ_c). In this study, we use gas volume fraction (V_g) to represent magma porosity and assume that magma becomes permeable and degasses as it reaches the percolation threshold. The value of ϕ_c is widely variable, ranging from $\sim$ 17-78 vol%, due to the complex interplay between magma properties and physical processes such as melt viscosity and decompression rate (Rust & Cashman, 2011; Burgisser et al., 2017; Colombier et al., 2020). For melts with low viscosity and overpressure, such as the basaltic melts considered here, bubbles can grow and rise buoyantly, which reduces the likelihood of the bubbles coalescing to form a porous network. Colombier et al. (2020) suggest that low viscosity melts would become permeable at $\phi_c > 37$ vol% and we use that threshold here.

198 ## 3.2 Linking magma properties to observable parameters

199 ### *3.2.1 Deformation*

200 Satellite-based observations of subsurface volume change (derived from inverting
201 measurements of surface deformation) may be compared to the model of magma prop-
202 erties during degassing. We define the normalised volume change, $\bar{V}$, as the ratio between
203 the subsurface volume change (ΔV_c) and the volume erupted (V_e; assuming dense-rock
204 equivalent, DRE):

205 $$\bar{V} = \frac{\Delta V_c}{V_e} = (1 + \frac{\beta_m}{\beta_c})^{-1}, \tag{4}$$

206 where β_m is magma compressibility and β_c is chamber compressibility (Rivalta & Segall,
207 2008; Kilbride et al., 2016). Note that the definition of $\bar{V}$ is the inverse of that from Kilbride
208 et al. (2016), i.e., r = $\bar{V}^{-1}$. In an elastic half-space, chamber compressibility is affected
209 by host rock properties and chamber geometry, which can be defined as

210 $$\text{Spherical point source:} \quad \beta_c = \frac{3}{4\mu} \tag{5}$$

211 $$\text{Prolate chamber:} \quad \beta_c = \frac{1}{\mu} \tag{6}$$

212 $$\text{Horizontal oblate ellipsoid (sill):} \quad \beta_c = \frac{1}{\mu}(\frac{a}{c}\frac{3}{2\pi} - \frac{3}{5}) \tag{7}$$

213 where μ is the shear modulus of the crust and $\frac{a}{c}$ is the ratio of major to minor semi-axes
214 of an oblate ellipsoid (Amoruso & Crescentini, 2009; Anderson & Segall, 2011).

215 For compressible magmas, ΔV_c would be less than V_e (i.e., $\bar{V} < 1$), such that com-
216 pressible magmas with low ${}^{\beta_c}/_{\beta_m}$ have low volume change per unit erupted (Voight et
217 al., 2010), while ΔV_c would be approximately equal to V_e (i.e., $\bar{V} \approx 1$) for incompress-
218 ible magmas and high ${}^{\beta_c}/_{\beta_m}$. Since chamber geometry and host rock properties also af-
219 fect β_c and hence the magnitude of $\bar{V}$, volcanoes with compressible magmas and rigid
220 surrounding crust (i.e., high μ and low β_c) cause small volume changes during an erup-
221 tion (Rivalta & Segall, 2008; Kilbride et al., 2016).

222 A directly observable parameter is surface deformation. Here we define normalised
223 displacement $\bar{z}$ as the maximum vertical displacement per unit volume erupted. For sim-
224 plicity, we only calculate the normalised displacement for a spherical point source in a
225 uniform and elastic half-space (Mogi, 1958), $\bar{z} = \bar{V}\ \frac{1-v}{\pi}\ \frac{1}{d^2}$, where v is Poisson′s ratio
226 and d is the depth of magma chamber, although other models are also available (Okada,

1985; Yang et al., 1988; Fialko et al., 2001; Masterlark, 2003; Albino et al., 2019; Zhan et al., 2019). $\bar{z}$ is vertically above the source of deformation.

3.2.2 Degassing

Observations of SO_2 degassing are made by satellite-based sensors (e.g., Prata & Kerkmann, 2007; Carn et al., 2016; Theys et al., 2019). We define normalised SO_2 ($\bar{S}$) as the observed SO_2 emitted (E^{SO_2}), normalised by the volume of magma erupted (V_e). $\bar{S}$ estimates the mass of SO_2 per unit volume of magma:

$$\bar{S} = \frac{E^{SO_2}}{V_e} = \frac{m^{SO_2} M^{SO_2} \rho_e w_g}{M_g}, \tag{8}$$

where m^{SO_2} is the mole fraction of SO_2 in gaseous phase, M^{SO_2} is the molecular mass of SO_2, $\rho_e = 2800\ \mathrm{kg\,m^{-3}}$ is the erupted rock density, and M_g is the mean molecular mass of the gas phase. For explosive eruptions, we assume that the mass of SO_2 emissions at the surface (E^{SO_2}) is the same as the mass of SO_2 in equilibrium with magma at chamber depth, meaning that there is no additional degassing as magma rises from the chamber to the surface (Figure 1b). For effusive eruptions, volatiles exsolve in the conduit as magma ascends slowly such that SO_2 degassing is dominated by co-eruptive degassing (Figure 1c). For simplicity, we assume all exsolved SO_2 is emitted as SO_2 in the plume (i.e., there are no other sulfur-bearing species present) and that all SO_2 can be detected by satellites. We ignore sulfur loss due to leaching, sulfur scrubbing by hydrothermal systems, and the formation of sulfide globules during sulfide saturation.

4 One-at-a-time Sensitivity Tests

In this section, we explore the sensitivity of the calculated magma properties to initial magmatic H_2O content (w^{H_2O}), magmatic CO_2 content (w^{CO_2}), oxygen fugacity (f_{O_2}), magmatic S content (w^S), crustal shear modulus (μ) and chamber geometry. We conduct one-at-a-time sensitivity tests by holding other parameters constant and varying the chosen parameter. For each example, we first consider the general sensitivity of the model to changing magma properties by looking at the maximum percentage changes over a range of depths, and then provide an illustrative example for a chamber at a depth of 3 km (i.e., pressure of 82 MPa). While this provides a clear understanding of the role

Table 1. Volatile composition of the parameters explored. The sensitivity tests vary the chosen parameter (bracketed) while holding all other parameters constant (unbracketed).

Parameters	H_2O (wt%)	CO_2 (ppm)	f_{O_2}	S (ppm)
Sensitivity test	2.0∗ (1.0-3.0)	1000 (500 − 1500)	NNO (NNO − 1-NNO + 1)	2000 (1000-3000)

*All sensitivity tests use constant w^{H_2O} = 2.0 wt%, except for S, which uses w^{H_2O} = 3.0 wt%.

of each parameter, it does not consider the co-dependence of input variables, which may result in parameter combinations that are not physically realistic.

Bulk magma volatile contents are informed by observations of dissolved volatile content from melt inclusions of basalts. For simplicity, we assume an isothermal magma at 1200 °C. We explore w^{H_2O}, w^{CO_2} and w^S in the ranges of 1.0 to 3.0 wt% H_2O, 500 to 1500 ppm CO_2, and 1000 to 3000 ppm S, respectively (Table 1). We use f_{O_2} from NNO−1 to NNO+1 to explore the effects of oxygen fugacity on the solubility of volatile species. To test how chamber compressibility (β_c) affects volcanic deformation, we use μ from 0.1 to 30 GPa (Heap et al., 2020), and consider three chamber geometries: a spherical point source, a vertical prolate ellipsoid (pipe-like chamber) and a horizontal oblate ellipsoid (sill) (Gudmundsson, 2008; Amoruso & Crescentini, 2009; Anderson & Segall, 2011). Although we do not expect the gas to remain in contact with the magma when V_g exceeds the percolation threshold at which magma becomes permeable, i.e., $\phi_c > 37$ vol% (Colombier et al., 2020), we run our sensitivity tests all the way to the surface. Table 2 summarises the maximum percentage change over the depth range of each parameter on the estimated values of $\bar{S}$, $\bar{V}$ and $\bar{z}$.

4.1 Effects of H_2O content on magma properties

First, we vary the initial dissolved H_2O content w^{H_2O} in the melt and investigate how it affects magma properties ρ_m and β_m, and observables $\bar{S}$, $\bar{V}$ and $\bar{z}$ (Figure 2) during ascent and degassing. In this sensitivity test, w^{H_2O} ranges from 1.0-3.0 wt% and the constant parameters are w^{CO_2} = 1000 ppm, f_{O_2} = NNO, w^S = 2000 ppm. We assume a fixed chamber compressibility for a spherical cavity $\beta_c = \frac{3}{4\mu}$ where μ = 2.1 GPa (i.e., $\beta_c = 3.6\times10^{-10}$ Pa^{-1}).

Solubility decreases with decreasing pressure for each volatile component, so as pressure decreases, the mass fraction dissolved in the melt (w_M^x) decreases and the mole frac-

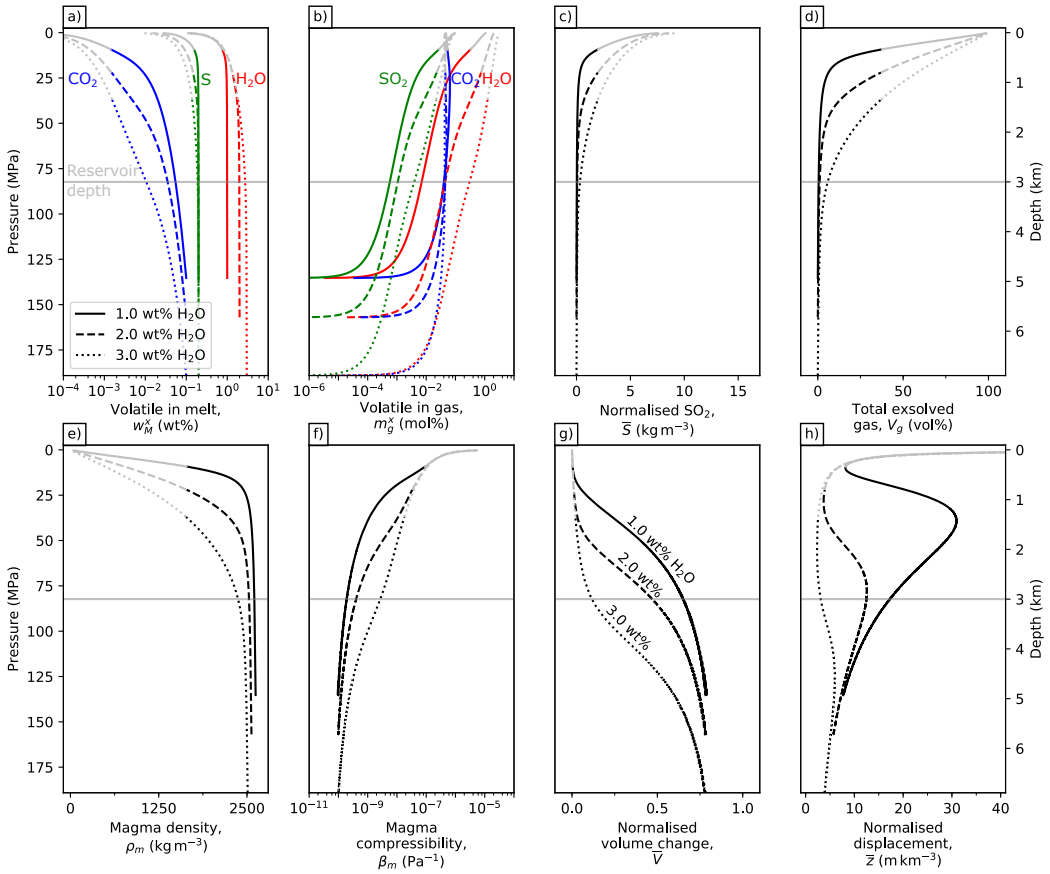

Figure 2. Physicochemical properties of basalts when varying the initial magmatic H_2O from 1.0-3.0 wt%. (a) Weight fraction of dissolved H_2O, CO_2 and S in melt (w_M^x). (b) Mole fraction of exsolved H_2O, CO_2 and SO_2 in gas (m_g^x). (c) Mass of SO_2 gas per unit volume of magma, also defined as normalised SO_2 ($\bar{S}$). (d) Volume fraction of exsolved gases in magma (V_g). (e) Magma density (ρ_m). (f) Magma compressibility (β_m). (g) Model predicted volume change normalised by unit volume of magma ($\bar{V}$). (h) Maximum vertical displacement normalised by unit volume of magma ($\bar{z}$). The grey lines represent magma properties after exceeding percolation threshold $\phi_c = 37$ vol%. Fixed parameters: $w^{CO_2} = 1000$ ppm, $f_{O_2} = $ NNO, $w^S = 2000$ ppm and $\mu = 2.1$ GPa.

Table 2. Summary table showing the maximum percentage change of each observation when increasing the values of each parameter (shown in brackets) while holding other parameters constant.

Parameters	Normalised SO_2, $\bar{S}$ ($kg\,m^{-3}$)	Normalised volume change, $\bar{V}$	Normalised displacement, $\bar{z}$ ($m\,km^{-3}$)
Magmatic H_2O, w^{H_2O} (1.0-3.0 wt%)	+370%	−83%	−92%
Magmatic CO_2, w^{CO_2} (500-1500 ppm)	+74%	−37%	−44%
Oxygen fugacity, f_{O_2} (NNO−1-NNO+1)	+110%	+15%	+17%
Magmatic S, w^S (1000-3000 ppm)	+130%	−5.3%	−0.35%
Crustal shear modulus, μ (0.1-30 GPa)	n/a	−94%	−98%

tion that has exsolved to the gaseous phase (m_g^x) increases (Figure 2a-b). Higher w^{H_2O} reduces the solubility of CO_2 and S (Figure 2a), thus increasing the mole fraction of $m_g^{H_2O}$, $m_g^{CO_2}$ and m_g^S (Figure 2b). Normalised SO_2 ($\bar{S}$) represents the mass of exsolved SO_2 per unit volume of magma, assuming that melt and gas do not segregate. By increasing w^{H_2O} by a factor of 3, $\bar{S}$ increases up to a maximum of $\sim$ 370% at 0.51 km depth (Figure 2c). Gas volume fraction (V_g) increases as volatiles exsolve and gas bubbles expand at lower pressures. Since V_g is dominated by w^{H_2O}, V_g increases up to a maximum of $\sim$ 440% at 0.58 km depth when increasing w^{H_2O} from 1.0 to 3.0 wt% (Figure 2d).

The increase in w^{H_2O} increases V_g, which decreases magma density (ρ_m; Equation 2; Figure 2e) and increases magma compressibility (β_m; Equation 3; Figure 2f). Therefore, with the increase of w^{H_2O} from 1-3 wt%, β_m increases up to a maximum of $\sim$ 1900% at 2.1 km depth (Figure 2f), and normalised volume change ($\bar{V}$) decreases up to a maximum of $\sim$ 83% at 2.9 km depth (Figure 2g). Based on the simple Mogi model, there is a trade-off between volume change and depth, such that the same volume change will cause a larger displacement at a shallow depth. However, when V_g and β_m are considered, the maximum vertical displacement per unit volume ($\bar{z}$) does not vary in a simple way; the increase in V_g towards the surface causes a local minimum in $\bar{z}$ at 0.5 km depth. Given that $\bar{z}$ is controlled by chamber depth and $\bar{V}$, increasing w^{H_2O} thus causes a relative decrease in the normalised displacement ($\bar{z}$) up to a maximum of $\sim$ 92% at 1.4 km depth (Figure 2h).

To illustrate these results, we give specific values for a chamber depth of 3 km. Varying w^{H_2O} from 1.0 to 3.0 wt% increases $\bar{S}$ from 0.025 kg m^{-3} to 0.32 kg m^{-3} (Figure 2c). V_g increases from 0.47 vol% to 5.8 vol%, which corresponds to the increase in β_m from 1.9×10^{-10} Pa^{-1} to 27×10^{-10} Pa^{-1} (Figure 2f). As a result, $\bar{V}$ decreases from 0.65 to 0.11 (Figure 2g) and $\bar{z}$ is reduced from 17 m km^{-3} to 3.1 m km^{-3} (Figure 2h). The model thus predicts that basalts with higher initial H_2O content have greater $\bar{S}$ and β_m, and as a result, lower $\bar{V}$ and $\bar{z}$ (Figure 2).

4.2 Effects of CO_2 content on magma properties

Here, we vary initial dissolved CO_2 content to understand how it affects magma properties and observables $\bar{S}$, $\bar{V}$ and $\bar{z}$ (Figure 3). We use w^{CO_2} in the range of 500 ppm to 1500 ppm and fixed $w^{H_2O} = 2.0$ wt%, f_{O_2} = NNO, $w^S = 2000$ ppm and $\mu = 2.1$ GPa for this model.

Figure 3a shows that increasing w^{CO_2} from 500 ppm to 1500 ppm increases the amount of dissolved $w_M^{CO_2}$ up to a maximum of 55% at 1.5 km depth, but decreases $w_M^{H_2O}$ and w_M^S by <5.3% and <4.1%, respectively. This results in a relative increase in the amount of exsolved SO_2 ($m_g^{SO_2}$) and $\bar{S}$ up to a maximum of ∼80% and ∼74%, respectively, at 1.5 km depth (Figure 3b-c). Similarly, varying initial CO_2 content increases V_g up to a maximum of ∼72% at 1.5 km depth (Figure 3d). Increasing w^{CO_2} corresponds to an increase in β_m up to a maximum of <54% and a decrease in $\bar{V}$ up to a maximum of 37% at 2.9 km depth (Figure 3f-g), which correlates to the decrease in $\bar{z}$ up to a maximum of 44% at 2.5 km depth (Figure 3h).

Here, we quantify these results for a depth of 3 km to illustrate the sensitivity to w^{CO_2}. Increasing initial CO_2 from 500 ppm to 1500 ppm increases $\bar{S}$ from 0.014 kg m^{-3} to 0.10 kg m^{-3} and V_g from 0.26 vol% to 1.9 vol% (Figure 3c-d). This corresponds to an increase in β_m from 2.3×10^{-10} Pa^{-1} to 5.6×10^{-10} Pa^{-1} (Figure 3f). As a result, $\bar{V}$ decreases from 0.61 to 0.39 (Figure 3g). and $\bar{z}$ is reduced from 16 m km^{-3} to 10 m km^{-3} (Figure 3h). The model shows that increasing initial CO_2 content from 500 ppm to 1500 ppm causes significant changes to both $\bar{V}$ and $\bar{z}$, but they are approximately half that of varying w^{H_2O} from 1.0 wt% to 3.0 wt%. As such, variations in H_2O content have a greater effect on co-eruptive deformation than variations in CO_2 content.

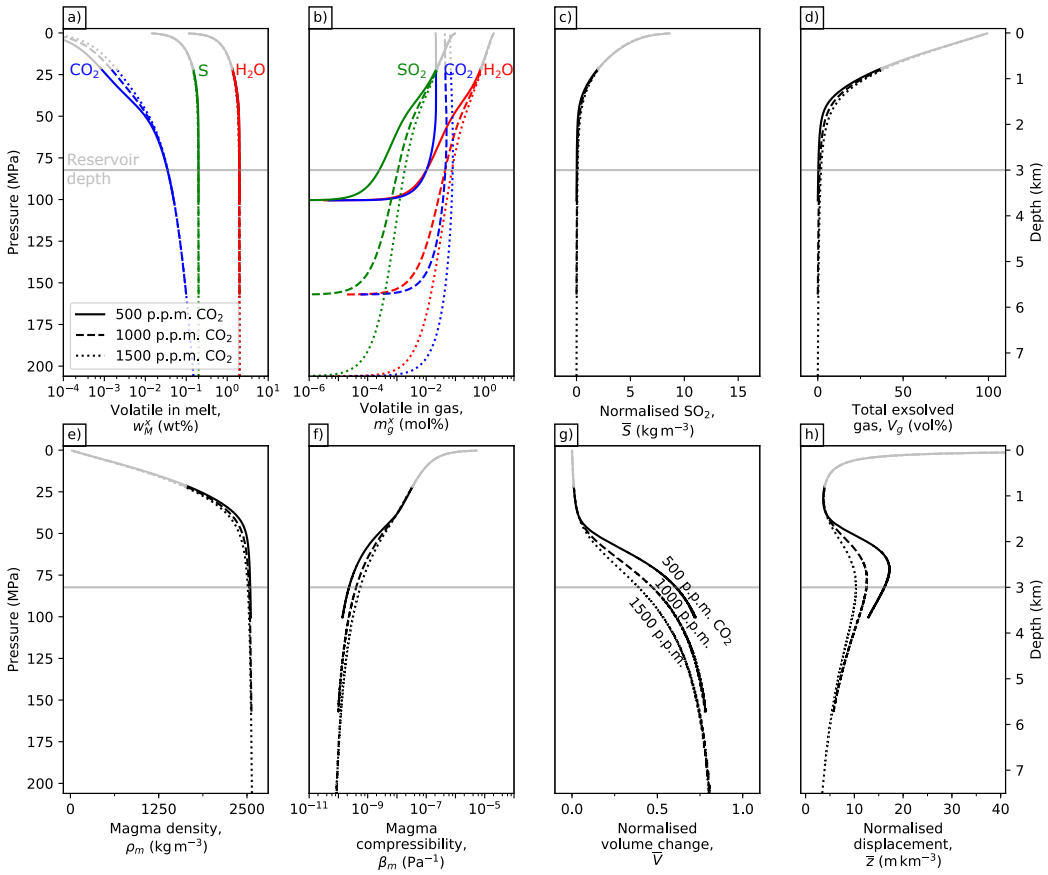

Figure 3. Physicochemical properties of basalts when varying the initial weight fraction of dissolved CO_2 (w^{CO_2}) from 500 to 1500 ppm. (a) Weight fraction of dissolved H_2O, CO_2 and S in melt (w_M^x). (b) Mole fraction of exsolved H_2O, CO_2 and SO_2 in gas (m_g^x). (c) Mass of SO_2 gas per unit volume of magma, also defined as normalised SO_2 ($\bar{S}$). (d) Volume fraction of exsolved gases in magma (V_g). (e) Magma density (ρ_m). (f) Magma compressibility (β_m). (g) Model predicted volume change normalised by unit volume of magma ($\bar{V}$). (h) Maximum vertical displacement normalised by unit volume of magma ($\bar{z}$). The grey lines represent magma properties after exceeding percolation threshold $\phi_c = 37$ vol%. Fixed parameters: $w^{H_2O} = 2.0$ wt%, $f_{O_2} =$ NNO, $w^S = 2000$ ppm and $\mu = 2.1$ GPa.

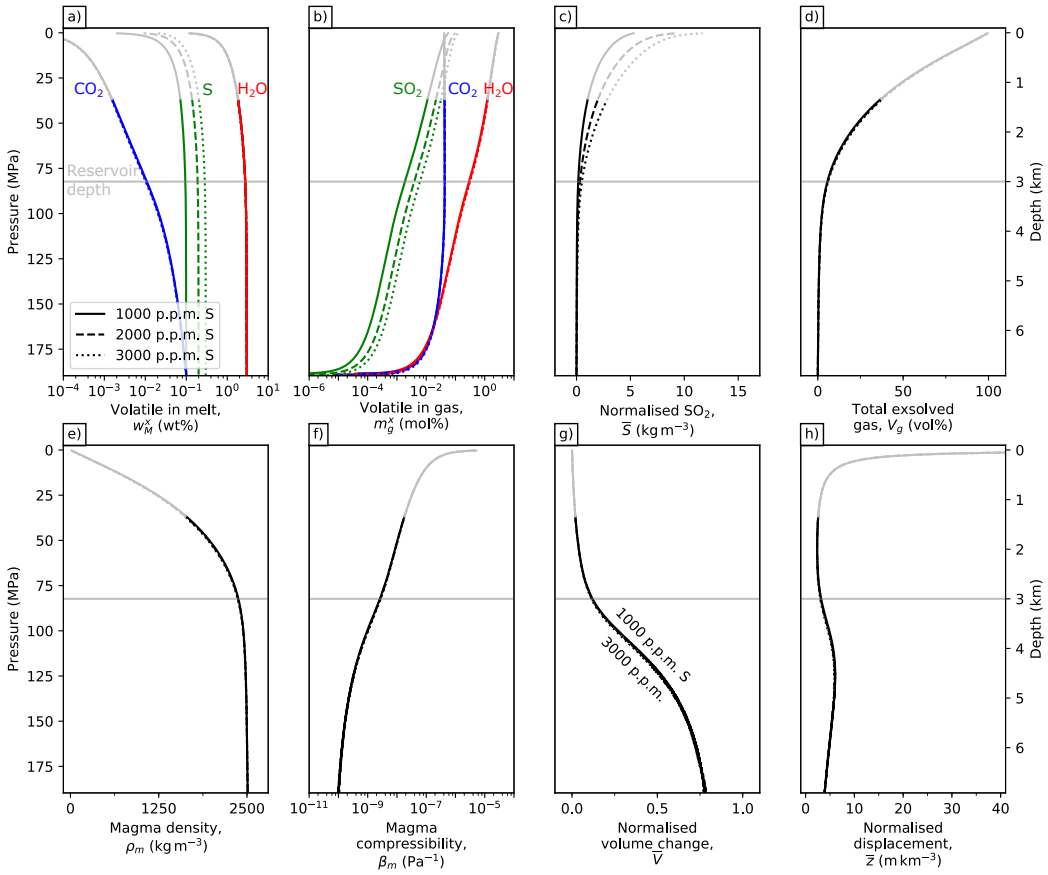

Figure 4. Physicochemical properties of basalts when varying the initial weight fraction of dissolved S (w^{S}) from 1000 to 3000 ppm. (a) Weight fraction of dissolved H_2O, CO_2 and S in melt (w_M^x). (b) Mole fraction of exsolved H_2O, CO_2 and SO_2 in gas (m_g^x). (c) Mass of SO_2 gas per unit volume of magma, also defined as normalised SO_2 ($\bar{S}$). (d) Volume fraction of exsolved gases in magma (V_g). (e) Magma density (ρ_m). (f) Magma compressibility (β_m). (g) Model predicted volume change normalised by unit volume of magma ($\bar{V}$). (h) Maximum vertical displacement normalised by unit volume of magma ($\bar{z}$). The grey lines represent magma properties after exceeding percolation threshold $\phi_c = 37$ vol%. Fixed parameters: $w^{\mathrm{H_2O}} = 3.0$ wt%, $w^{\mathrm{CO_2}} = 1000$ ppm, $f_{\mathrm{O_2}}$ = NNO and $\mu = 2.1$ GPa.

4.3 Effects of sulfur content

Here, we vary initial dissolved sulfur (S) content to understand how it affects magma properties and observables $\bar{S}$, $\bar{V}$ and $\bar{z}$ (Figure 4). We use w^{S} in the range of 1000 ppm to 3000 ppm and fixed $w^{\mathrm{H_2O}} = 3.0$ wt%, $w^{\mathrm{CO_2}} = 1000$ ppm, $f_{\mathrm{O_2}} = \mathrm{NNO}$ and $\mu = 2.1$ GPa for this model.

Figure 4a shows that w_M^{S} increases by <200% at 6.9 km depth with increasing w^{S} from 1000 ppm to 3000 ppm, which corresponds to the increase in $m_g^{\mathrm{SO_2}}$ and $\bar{S}$ up to a maximum of ∼138% and ∼130% at the surface, respectively (Figure 4b-c). The total gas volume fraction, however, increases by only <3% at 1.4 km depth (Figure 4d). Since varying initial S content has minimal impact on V_g, β_m only increases by <9.3% at 3.6 km depth (Figure 4f), which correlates to the decrease in $\bar{V}$ by less than 5.3% at 3.9 km depth and $\bar{z}$ less than 0.35% at the surface (Figure 4g-h).

We quantify these results for a depth of 3 km to illustrate the effect of varying w^{S} from 1000 ppm to 3000 ppm. This range of sulfur is less than the sulfur content at sulfide saturation. Increasing magmatic w^{S} increases $\bar{S}$ from 0.15 $\mathrm{kg\,m^{-3}}$ to 0.50 $\mathrm{kg\,m^{-3}}$ (Figure 4c), which can be linked to the increase in V_g from 5.6 vol% to 6.0 vol% (Figure 4d). This corresponds to a very small increase in β_m from $2.6{\times}10^{-9}$ $\mathrm{Pa^{-1}}$ to $2.8{\times}10^{-9}$ $\mathrm{Pa^{-1}}$ (Figure 4f). The increase in β_m thus reduces both $\bar{V}$ and $\bar{z}$ marginally from 0.12 to 0.11 and 3.2 $\mathrm{m\,km^{-3}}$ to 3.0 $\mathrm{m\,km^{-3}}$, respectively (Figure 4g-h). The model shows that basalts with high initial w^{S} release high $\bar{S}$ but β_m and hence co-eruptive deformation is only minimally affected.

4.4 Effects of oxygen fugacity on magma properties

Figure 5 shows how varying oxygen fugacity ($f_{\mathrm{O_2}}$) affects magma properties, and consequently observables $\bar{S}$, $\bar{V}$ and $\bar{z}$. We vary $f_{\mathrm{O_2}}$ from NNO−1 to NNO+1 and fix $w^{\mathrm{H_2O}}$ = 2.0 wt%, $w^{\mathrm{CO_2}} = 1000$ ppm, $w^{\mathrm{S}} = 2000$ ppm and $\mu = 2.1$ GPa for this model.

The model predicts that varying $f_{\mathrm{O_2}}$ from NNO−1 to NNO+1 increases $w_M^{\mathrm{CO_2}}$, $w_M^{\mathrm{H_2O}}$ and w_M^{S} up to a maximum of 2.3%, 9.0% and 32% at depths of 2.9, 7.1 and 2.1 km, respectively, due to the effect of oxygen fugacity on the solubility of each volatile species (Figure 5a). The significant increase in w_M^{S} causes a relative increase $m_g^{\mathrm{SO_2}}$ and $\bar{S}$ up to a maximum of 119% and 112%, respectively, at 0.4 km depth (Figure 5b-c).

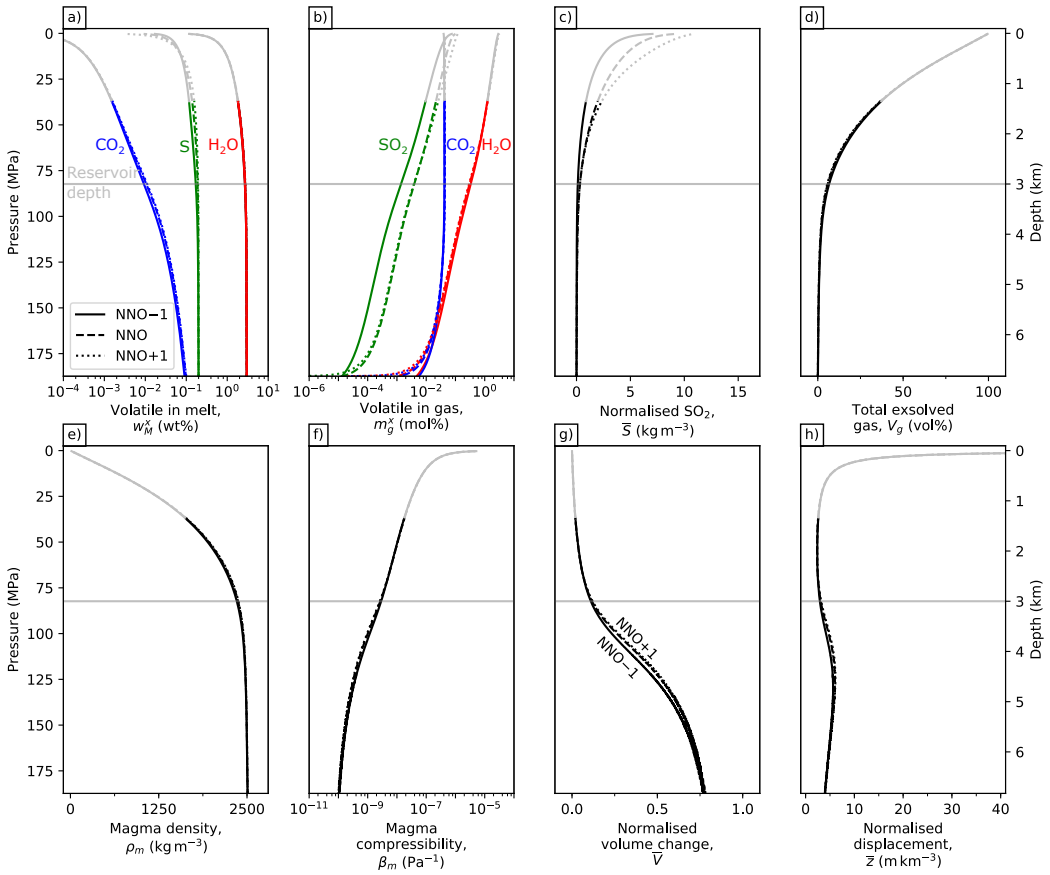

Figure 5. Physicochemical properties of basalts when varying f_{O_2} of magma storage from NNO−1 to NNO+1. (a) Weight fraction of dissolved H_2O, CO_2 and S in melt (w_M^x). (b) Mole fraction of exsolved H_2O, CO_2 and SO_2 in gas (m_g^x). (c) Mass of SO_2 gas per unit volume of magma, also defined as normalised SO_2 ($\bar{S}$). (d) Volume fraction of exsolved gases in magma (V_g). (e) Magma density (ρ_m). (f) Magma compressibility (β_m). (g) Model predicted volume change normalised by unit volume of magma ($\bar{V}$). (h) Maximum vertical displacement normalised by unit volume of magma ($\bar{z}$). The grey lines represent magma properties after exceeding percolation threshold $\phi_c = 37$ vol%. Fixed parameters: $w^{H_2O} = 2.0$ wt%, $w^{CO_2} = 1000$ ppm, $w^{S} = 2000$ ppm and $\mu = 2.1$ GPa.

However, V_g is reduced by only <11% at 2.8 km depth so varying f_{O_2} has minimal impact on ρ_m and β_m (Figure 5e). In fact, increasing f_{O_2} from NNO−1 to NNO+1 decreases β_m by 20% at 4.2 km depth (Figure 5f) and hence $\bar{V}$ of oxidised basalts is <15% greater than its reduced counterpart at 4.2 km depth (Figure 5g). While $\bar{z}$ is controlled by chamber depth and $\bar{V}$, the maximum increase in $\bar{z}$ of less than 17% also occur at 4.2 km depth due to insignificant difference in $\bar{V}$ when varying f_{O_2} (Figure 5h).

Next, we quantify the predictions for a depth of 3 km. Varying f_{O_2} from NNO−1 to NNO+1 increases $\bar{S}$ from 0.11 kg m^{-3} to 0.31 kg m^{-3} (Figure 5c). However, V_g decreases from 6.6 vol% to 5.5 vol%, which corresponds to a decrease in β_m from 2.9×10^{-10} Pa^{-1} to 2.6×10^{-10} Pa^{-1} (Figure 5f). As a result, $\bar{V}$ and $\bar{z}$ increases from 0.11 to 0.12 and 2.9 m km^{-3} to 3.2 m km^{-3}, respectively (Figure 5g-h). The model thus predicts that while oxidised basalts have greater $\bar{S}$ than reduced basalts, variations in oxygen fugacity of basalts has minimal impact on co-eruptive deformation.

4.5 Effects of chamber compressibility

Crustal properties and chamber geometry are known to have a major role in determining surface deformation (e.g., Gudmundsson, 2008; Amoruso & Crescentini, 2009; Anderson & Segall, 2011; Heap et al., 2020). Here we investigate the two parameters that directly affect our simplified model using the same sensitivity analysis as for the other parameters. $\bar{V}$ is a function of β_m and β_c, and the two parameters we explore in this section are crustal shear modulus and chamber geometry that control β_c and thus affect $\bar{V}$ (Equation 4). We use a range of crustal shear modulus (μ) from 0.1 GPa (compliant crust) to 30 GPa (non-compliant crust), which is typical in volcanic areas (Gudmundsson, 2005; Rivalta & Segall, 2008). It is noted that μ changes with depth but for simplicity, we assume a constant μ at all depths considering the variations in and between volcanic regions are likely to be larger than those with depth. We considered three representative chamber geometries, which are a spherical point source, a vertical prolate ellipsoid (pipe-like chamber) and a horizontal oblate ellipsoid (sill), and use $\frac{a}{c} = 100$ for the horizontal sill (Equation 5) (Amoruso & Crescentini, 2009; Anderson & Segall, 2011). We use a Poisson′s ratio v of 0.30 based on the average value for volcanic rock with average porosity and fracture density (Heap et al., 2020). The sensitivity test uses fixed parameters of $w^{H_2O} = 2.0$ wt%, $w^{CO_2} = 700$ ppm, $f_{O_2} =$ NNO, and $w_g = 0.01$ wt%.

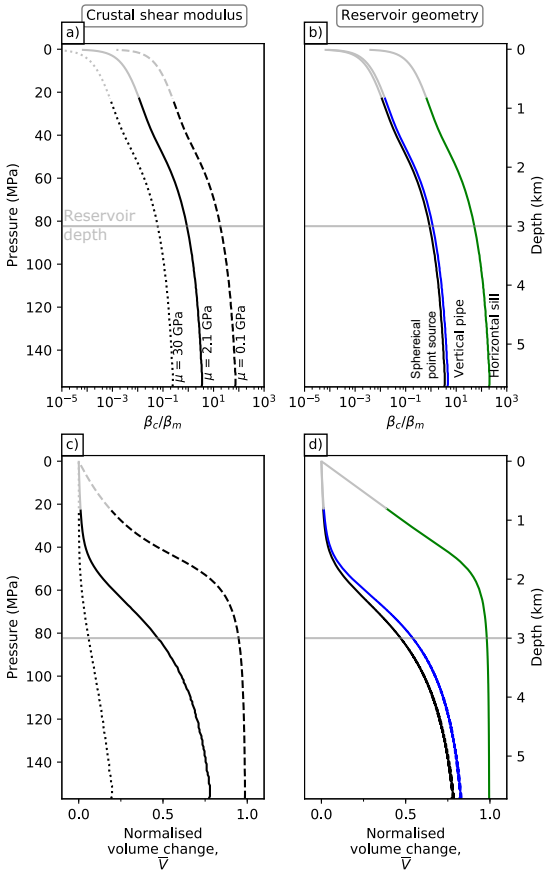

Figure 6. Physical properties of basalts when varying the crustal shear modulus (μ) from 0.1 to 30 GPa and chamber geometry. (a) The ratio of ${}^{\beta_c}/_{\beta_m}$ to illustrate the effects of crustal shear modulus and chamber geometry. The μ used are 0.1 GPa, 2.1 GPa and 30 GPa (Heap et al., 2020), and the chamber geometries considered are a spherical point source, a vertical pipe-like chamber and a horizontal sill (Amoruso & Crescentini, 2009). Different μ and chamber geometries are represented by different line styles and colour, respectively. (b) Model predicted normalised volume change ($\bar{V}$) for a spherical point source, a vertical pipe-like chamber and a horizontal sill with $\mu = 2.1$ GPa. The major to minor semiaxis of the horizontal sill, $\frac{a}{c}$, is 100. (c) $\bar{V}$ for a spherical point source with varying μ. (d) $\bar{V}$ for a spherical point source, a vertical pipe-like chamber and a horizontal sill with $\mu = 2.1$ GPa. Fixed parameters: $w^{\mathrm{H_2O}} = 2.0$ wt%, $w^{\mathrm{CO_2}} = 1000$ ppm, $f_{\mathrm{O_2}} = \mathrm{NNO}$, and $w^{\mathrm{S}} = 2000$ ppm. The grey lines represent magma properties when percolation threshold exceeds $\phi_c = 37$ vol%.

To understand how crustal properties affect volcanic deformation, we first discuss the effects of μ and chamber geometry on the ratio of ${}^{\beta_c}/_{\beta_m}$. Since β_c is inversely proportional to μ, a crust with $\mu = 0.1$ GPa results in ${}^{\beta_c}/_{\beta_m} = 19$ for a chamber at 3 km depth, while ${}^{\beta_c}/_{\beta_m} = 0.062$ for a crust with $\mu = 30$ GPa (Figure 6a). From Equation 5, we find that the crustal compressibility β_c for chambers with a vertical pipe-like shape is 33% higher than a spherical point source (Figure 6b). An ellipsoid with $\frac{a}{c} = 100$ has the highest β_c among the three chamber geometries (i.e., 60 times greater than a spherical point source), consistent with analytical results from Anderson and Segall (2011).

Here we quantify the effects of varying μ and the chamber geometry on $\bar{V}$ (Figure 6c-d). The $\bar{V}$ for crustal rocks with $\mu = 0.1$ GPa is up to a maximum of $\sim 360\%$ greater than that with $\mu = 2.1$ GPa at 2.1 km depth. In contrast, $\bar{V}$ is reduced up to a maximum of $\sim 74\%$ at 5.7 km depth for a crust with $\mu = 30$ GPa when compared to $\mu =$ 2.1 GPa. At 3 km depth, the $\bar{V}$ for $\mu = 0.1$ GPa, 2.1 GPa and 30 GPa are 0.95, 0.47 and 0.058, respectively (Figure 6c). The effects of different chamber geometries on $\bar{V}$ are shown in Figure 6d, with $\mu = 2.1$ GPa and Poisson′s ratio v of 0.30 (Heap et al., 2020). The normalised volume change $\bar{V}$ is greatest for horizontal sills and smallest for spherical point source, such that $\bar{V} = 0.98$ and 0.47, respectively, for a chamber at 3 km depth. Based on the effects of μ and chamber geometry on ${}^{\beta_c}/_{\beta_m}$, we find that a volcano with low ${}^{\beta_c}/_{\beta_m}$ (i.e., spherical, high shear modulus) has low $\bar{V}$ which indicates muted volcanic deformation. In contrast, a volcano with high ${}^{\beta_c}/_{\beta_m}$ (i.e., horizontal sill, low shear modulus) has high $\bar{V}$. For example, at 3 km depth, $\bar{V} = 0.058$ for a spherical point source with $\mu =$ 30 GPa, but $\bar{V} = 1.0$ for a sill with $\mu = 0.1$ GPa.

The main takeaways from the sensitivity analysis of chamber compressibility is that 1) spherical point sources and vertical pipe-like chambers have similar ${}^{\beta_c}/_{\beta_m}$ and $\bar{V}$, whereas sills have higher ${}^{\beta_c}/_{\beta_m}$ and thus high $\bar{V}$ (Figure 6b,d) and 2) crustal properties, specifically shear modulus, have a significant influence on $\bar{V}$, with lower crustal shear modulus causing larger volume changes (Figure 6a,c) (Heap et al., 2020; Hautmann et al., 2010).

4.6 Summary of sensitivity analyses

Here we summarise the results from each sensitivity test. A summary of the maximum percentage change of $\bar{S}$, $\bar{V}$ and $\bar{z}$ over the depth range of each parameter are shown in Table 2. We find that eruptions of water-rich magmas have higher SO_2 emissions and

less deformation for a particular volume of magma erupted. While initial magmatic CO_2 causes insignificant changes to the total amount of SO_2 degassing during eruptions, it has a moderate influence on the observed co-eruptive deformation, i.e., CO_2-rich magmas are more compressible. Initial magmatic S and oxygen fugacity have a strong influence on the magnitude of SO_2 degassing but have a minimal impact on the magnitude of the co-eruptive deformation. Magmas with a high oxygen fugacity yield high SO_2 emissions during an eruption, but this does not impact co-eruptive deformation significantly. Magmatic reservoirs with strong surrounding crustal rocks (i.e., high μ) and spherical geometry may display muted co-eruptive deformation.

5 Comparison Between Arc Basalts and Ocean Island Basalts

5.1 Thermodynamic modelling of magma properties

We now examine how tectonic setting influences the physicochemical properties of basaltic magma and consequently its impact on observed volcanic deformation and SO_2 degassing. Here we compare arc basalts and ocean island basalts by considering realistic parameter combinations and the co-dependence of parameters. Basaltic magma in arc settings tends to have higher water contents than basaltic magma from ocean island settings (e.g., Wallace, 2005; Zimmer et al., 2010; Plank et al., 2013). Melt inclusions data suggest that, on average, arc basalts contain 3.3 wt% H_2O, 1000 ppm CO_2 and 1200 ppm S, and ocean island basalts contain 1.0 wt% H_2O, 500 ppm CO_2 and 1100 ppm S (Wallace, 2005; Plank et al., 2013). These values represent the dissolved volatile abundances at shallow crustal levels, in which the volatiles recorded in the melt inclusions are primarily controlled by solubility. We note that arc basalts have been inferred to contain a minimum of 3000 ppm CO_2 from modelling of magma flux and melt inclusions (Wallace, 2005), but because primitive volatile contents are less well constrained, we selected the values from melt inclusions for simplicity. We take typical values of f_{O_2} of arc basalts and ocean island basalts from NNO-1 to NNO$+1$ and NNO-1.4 to NNO-0.4, respectively, based on examples from the Mexican Volcanic Belt and Kīlauea volcano (e.g., Carmichael & Ghiorso, 1986; Wallace & Carmichael, 1999). Crustal compressibility also influences the magnitude of volcanic deformation (Section 4.5), and thus we use $\mu = 2.1$ GPa, which is typical in volcanic areas, and assume a Mogi deformation source for simplicity (Mogi, 1958; Gudmundsson, 2005; Heap et al., 2020). The range of parameter values used for the analyses described below are listed in Table 3.

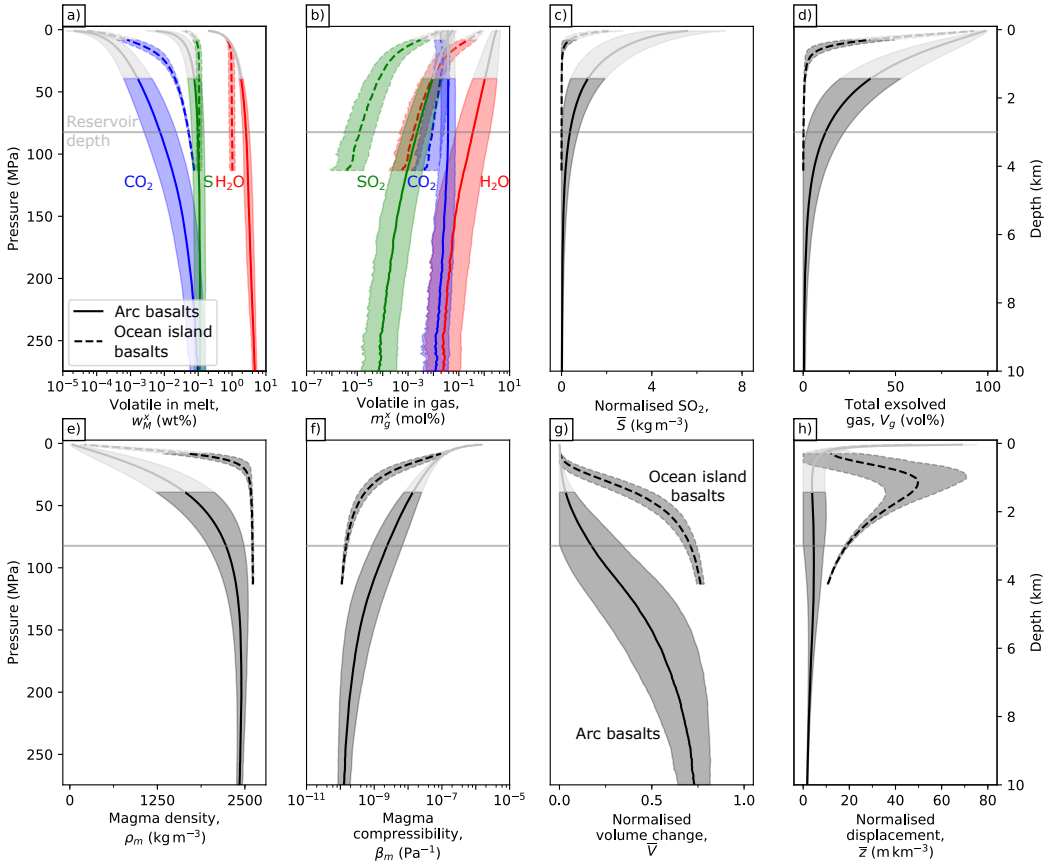

Figure 7. Comparison of magma properties between arc basalts (full line) and ocean island basalts (dashed line). The input parameters for the thermodynamic model ($w^{\mathrm{H_2O}}$, $w^{\mathrm{CO_2}}$ w^{S} and $f_{\mathrm{O_2}}$) and crustal shear modulus μ are initialised using a Monte-Carlo approach (Table 3). 1000 simulations are performed and the magma properties are calculated using the thermodynamic framework. (a) Weight fraction of dissolved volatile contents and (b) mol fraction of exsolved volatile contents. (c) Normalised SO_2 $\bar{S}$. (d) Volume fraction of exsolved gases in magma (V_g). (e) Magma density (ρ_m) and (f) Magma compressibility (β_m). (g) Normalised volume change ($\bar{V}$). (h) Normalised vertical displacement ($\bar{z}$). The grey lines represent magma properties after exceeding percolation threshold $\phi_c = 37$ vol% and the shaded region represent 1σ uncertainty. Range of parameter values for arc basalts and ocean island basalts are listed in Table 3.

Table 3. Range of parameters used for Monte-Carlo simulation.

Magma	H_2O (wt%)	CO_2 (ppm)	S (ppm)	f_{O_2}
Arc basalts	3.3 ± 1.0	1000 ± 400	1200 ± 400	NNO $\pm$ 0.5
Ocean island basalts	1.0 ± 0.2	500 ± 200	1100 ± 200	NNO $- 1.1 \pm 0.3$

Monte-Carlo simulation allows repeated random sampling to estimate possible ranges of magma properties and observations of volcanic eruptions, and as such we use the magma composition of arc basalts and ocean island basalts to estimate the realistic range of magma properties. We performed 1000 simulations for each type using the distribution of each variable (w^{H_2O}, w^{CO_2}, w^S, f_{O_2}) provided in Table 3 as input parameters for the thermodynamic model. Parameters that are distributed below the detection limit are readjusted accordingly (i.e., $w^{H_2O} < 0$ wt%, $w^{CO_2} < 25$ ppm and $w^S < 50$ ppm are changed to $w^{H_2O} = 1.0$ wt%, $w^{CO_2} = 25$ ppm and $w^S = 50$ ppm, respectively. The thermodynamic model has a starting temperature of 1200 °C, a Poisson's ratio v of 0.30, and we find the starting pressure/depth using the saturation point of each melt composition. After 1000 Monte-Carlo simulations, we calculate the mean and the standard deviation for each model output, such as normalised SO_2, magma compressibility and normalised volume change. Since we started each simulation at the saturation point for that composition (see Section 3.1), we apply a filter to discard the values for any pressure/depth with less than 100 simulations.

In Figure 7 we present the model predictions for arc basalts and ocean island basalts to illustrate the effects of tectonic settings on magma properties and co-eruptive observations. Arc basalts have a saturation point of ≈10 km, which is higher than that of ocean island basalts at ≈4 km depth due to the fact that arc basalts have a higher magmatic volatile content than ocean island basalts. The high f_{O_2} environment of arc basalts will tend to produce more exsolved SO_2 at the expense of H_2S and S_2, whereas ocean island basalts, which have a lower f_{O_2}, have less exsolved SO_2 in the gas phase (Figure 7b). With a higher mole fraction of exsolved SO_2, the predicted $\bar{S}$ of arc basalts is higher than that of ocean island basalts (Figure 7c). The higher magmatic volatile content of arc basalts translates to a higher V_g (Figure 7d), suggesting that in general, arc basalts are more compressible than ocean island basalts (Figure 7f). The increased magma compressibility indicates that arc basalts have a lower $\bar{V}$ and $\bar{z}$ than ocean island basalts (Figure 7g-h).

Here we give specific values for arc basalts and ocean island basalts assuming a magma chamber at 3 km depth (Figure 7). If an explosive eruption (no co-eruptive degassing) should occur from a chamber at 3 km depth, the predicted $\bar{S}$ of arc basalts is 0.37 $\mathrm{kg\,m^{-3}}$, greater than that of ocean island basalts at 0.0011 $\mathrm{kg\,m^{-3}}$ (Figure 7c). For a chamber at 3 km depth, arc basalts are more compressible than ocean island basalts at $\beta_m = 2.2{\times}10^{-9}$ $\mathrm{Pa^{-1}}$ and $1.2{\times}10^{-10}$ $\mathrm{Pa^{-1}}$, respectively (Figure 7f), and thus arc basalts have $\bar{V} = 0.17$ and $\bar{z} = 4.6\,\mathrm{m\,km^{-3}}$ as compared to ocean island basalts that have $\bar{V} = 0.71$ and $\bar{z} = 19\,\mathrm{m\,km^{-3}}$. It is noted that ocean island basalts eruptions are usually effusive in nature (i.e., co-eruptive degassing; see Section 2), and thus we expect $\bar{S}$ to be dominated by decompressional degassing and hence much higher than predicted for chamber degassing alone.

5.2 Comparison to Satellite Observations

In this section, we compare the magma properties predicted by the thermodynamic framework with observations of eruptions to understand published catalogues of volcanic deformation and degassing.

5.2.1 Data Compilation

Observations of volcanic deformation and SO_2 degassing during an eruption depend on both the properties of the magma and crust. Here we compiled deformation and SO_2 degassing data for 94 volcanic eruptions during the satellite era (2005-2020) to understand how theoretical estimates from thermodynamic modelling compare with observed eruptions (Supplementary Table 1). The primary magma composition and the dates for past eruptions are drawn from the Global Volcanism Program (2013). The compilation only considers volcanoes of basaltic composition. For eruptions with poorly constrained starting or ending dates, particularly for long-lived eruptions, we select the dates at which significant eruptions occur such as the the 2018 eruptions of Kīlauea, Ambrym and Fuego (e.g., Neal et al., 2019; Hamling et al., 2019; Naismith et al., 2019).

We compile 23 episodes of pre- and co-eruptive deformation detected with InSAR from the published catalogues of Biggs and Pritchard (2017) and Ebmeier et al. (2018) and 58 satellite observations of SO_2 degassing from individual studies (Supplementary Table 1), published catalogues (Carn et al., 2016, 2017) and Global Volcanism Program (2013). For eruptions that are less well studied (e.g., Chikurachki, Pagan, Semisopochnoi),

a)

	Arc basalt	Ocean island basalt
Eruptions (2005–2020)	61	33
Satellite-detected deformation	7	16
Satellite-detected SO_2 degassing	25	33
Satellite-detected SO_2 degassing and deformation	4	16
Absence of satellite-detected SO_2 degassing and deformation	3	0

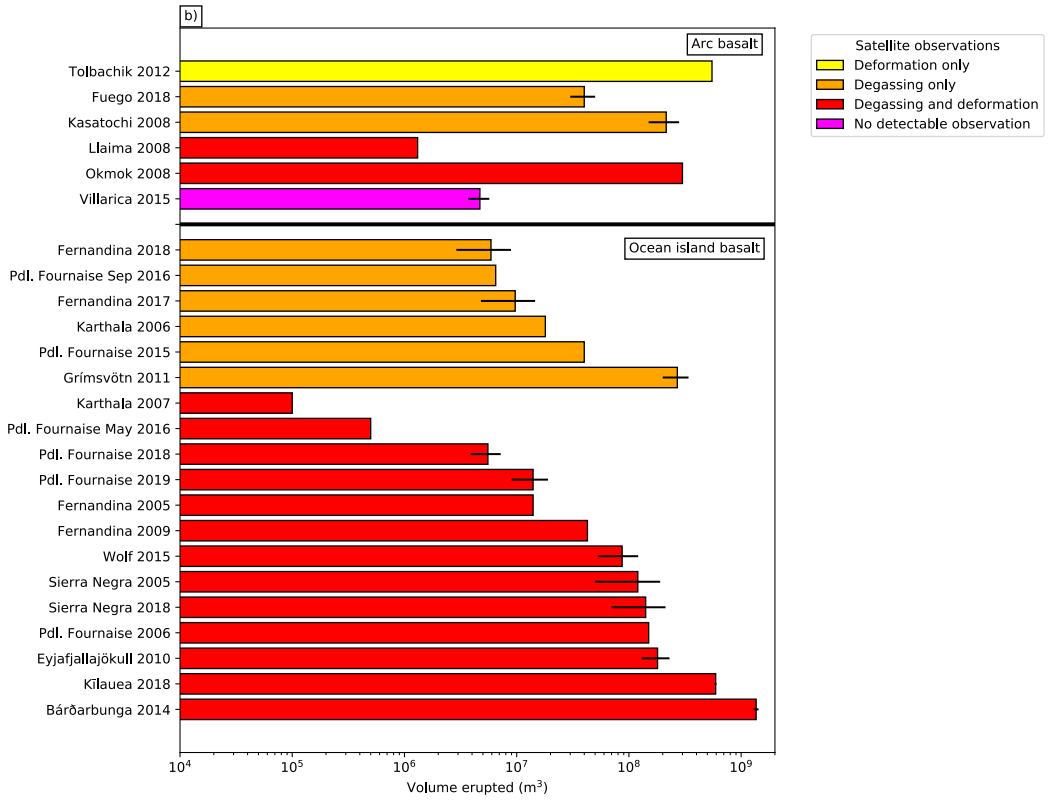

Figure 8. (a) Number of arc basalt and ocean island basalt eruptions with volcanic deformation (either uplift or subsidence) and SO_2 degassing measured by satellites during the satellite era (2005-2020). (b) Erupted volume for arc basalt and ocean island basalt eruptions. Columns are colour-coded for deformation and SO_2 degassing detectable by satellites. Uncertainties in the erupted volume, where available, are shown as horizontal error bars.

evidence for SO_2 degassing are crosschecked with the Global Sulphur Dioxide Monitoring homepage (https://so2.gsfc.nasa.gov/). Persistently degassing volcanoes (e.g., Shishaldin, Saunders, Korovin), including those whose emissions can be detected by satellites (e.g., Masaya, Miyakejima, Telica) (Carn et al., 2017), and submarine eruptions (e.g., Mayotte, Axial Seamount, Bristol Island) are not considered in this compilation. We also do not consider volcanoes that have approximately equal passive and eruptive SO_2 degassing regime such as Manam and Ulawun (Carn et al., 2016). We do, however, include eruptions that are significantly explosive (e.g., 2018 eruptions of Ambrym and Kīlauea).

We find that observations of deformation and SO_2 degassing are not available for every eruption despite similar erupted volume or volcano (Figure 8b). In fact, there is no clear correlation between satellite observations and erupted volume, consistent with previous studies (Kilbride et al., 2016), largely due to the challenges in volcano monitoring such as atmospheric noise, ice cover, or limitations in satellite sensors (e.g., OMI row anomaly for the 2012 eruption of Tolbachik). For example, satellite sensors could not measure the deformation associated with the 2011 eruption of Grimsvötn due to ice cover. Similarly, satellite measurement of SO_2 degassing is not available for the 2012-2013 eruption of Tolbachik, despite being one of the most voluminous arc basalt eruptions (Belousov et al., 2015), due to the OMI row anomaly (see https://so2.gsfc.nasa.gov/pix/daily/1112/kamchat_1112z.html).

Overall, deformation was detected at 25% of eruptions (23/94) and SO_2 degassing at 62% of eruptions (58/94)(Supplementary Table 1). A similar analysis conducted by Furtney et al. (2018) uses multiple satellite data spanning 1978-2016 to synthesise observations of volcanic deformation and degassing. Their study yielded similar results to ours: of the 250 volcanic eruptions between 1978-2016, 28% of eruptions have satellite observations of volcanic deformation, and SO_2 degassing is observed at 67% of eruptions (Furtney et al., 2018). The slightly higher proportion of volcanoes with satellite-detected deformation and degassing analysed by Furtney et al. (2018) is likely caused by the inclusion of pre- and post-eruptive observations. The overall proportion of satellite observations of volcanic deformation and SO_2 degassing appears to be fairly consistent between studies.

5.2.2 Comparison between tectonic settings

Our compilation shows that co-eruptive deformation has been observed at 48% of eruptions involving ocean island basalts (16/33), while only 11% of arc basalt eruptions had observed deformation (7/61) (Supplementary Table 1; Figure 8a). The lower frequency of detectable deformation at arc basalt eruptions can be attributed to the higher volatile contents of arc magmas, which our thermodynamic model predicts will increase magma compressibility and reduce surface deformation (Figure 7f-h). Systematic satellite observations of deformation spanning 1992-2010 analysed by Biggs et al. (2014) shows that the proportion of deforming volcanoes that erupted is higher for volcanoes in hotspot setting (66%; ocean island) as compared to those in subduction setting (53%; arc). For example, there are few InSAR observations from the Central American Volcanic Arc, where parental melts are water-rich (Ebmeier et al., 2013b; Wallace, 2005). Although this is an indirect comparison, the study agrees well with our results that observations of volcanic deformation are dominated by ocean island basalt eruptions. However, we note that other potential factors may also contribute to the lack of detectable deformation at volcanoes, independently or collectively (e.g. the rate of magma recharge, chamber geometry, depth of magma storage, viscoelastic crustal rheology, an open conduit, pre-eruptive degassing, atmospheric noise (Ebmeier et al., 2013b, 2013a; Chaussard et al., 2013; Head et al., 2019; Yip et al., 2019)) meaning that the models are very uncertain.

Volcanic SO_2 degassing was observed at all 33 ocean island basalt eruptions in our compilation but at only 41% of the arc basalt eruptions (25/61) (Supplementary Table 1; Figure 8a). While the higher magmatic volatile content of arc basalts might be expected to produce a higher detection rate(Figure 7c), the high rate of detection at ocean island basalt can be attributed to co-eruptive degassing. Conversely, the explosive nature of the arc basalt eruptions may mean there is there is no co-eruptive degassing and the only volatiles released are those in equilibrium at chamber depth. Additionally, technical difficulties in spectrometers, such as the 'row anomaly' in OMI that obscures the spectrometer's field of view (e.g., 2019 eruption of Klyuchevskoy, 2012 eruption of Tolbachik, 2010 eruption of Manam) prevents routine volcano monitoring.

We find that eruptions that have both satellite observations of volcanic deformation and degassing to be higher for ocean island basalt (16/33) as compared to arc basalt (4/61) (Figure 8a). Similarly, all ocean island basalts eruptions have been observed by at least one satellite sensor, while 3 of the 61 arc basalt eruptions were not detected by

either sensors. The lack of satellite observations for arc basalt eruptions highlights the difficulties in monitoring explosive eruptions with high magmatic volatile contents and thus compressible magmas (Huppert & Woods, 2002; Rivalta & Segall, 2008; Kilbride et al., 2016), and volcanoes with deep magma storage depth (Moran et al., 2006; Ebmeier et al., 2013b).

Finally, we further analyse 25 eruptions with erupted volume $\geq 1{\times}10^5$ m^3 (Figure 8b) to ensure comparable detection thresholds. All 19 ocean island basalt eruptions with erupted volume $\geq 1{\times}10^5$ m^3 have satellite observations of SO_2 degassing of which 13 have deformation measured by satellites (Figure 8b). For the case of arc basalt eruptions, we find no clear correlation between erupted volume $\geq 1{\times}10^5$ m^3 and satellite observations of SO_2 degassing and deformation (Figure 8b), in agreement with the wider catalogue and previous studies (Kilbride et al., 2016). This highlights the challenges for satellites to detect surface deformation, particularly for more evolved arc basaltic eruptions that are more compressible.

In summary, the thermodynamic framework and satellite observations of deformation agree well with each other such that volcanic deformation of volatile-poor ocean island basalt are more likely to be detected by satellites as compared to volatile-rich arc basalt (Figure 7g-h; Figure 8a). This is because volatile-rich arc basalts are highly compressibile, which results in muted surface deformation. Predictions of SO_2 degassing from our thermodynamic framework shows that volatile-rich arc basalts have greater SO_2 degassing, yet satellite observations show otherwise (Figure 7c; Figure 8a). We note that while the water content in arc basalts is two times greater than that of ocean island basalts, the sulfur content in basalts from both tectonic settings are similar (Table 3). The relationship between volatile content in basalts and satellite detections of SO_2 degassing suggests that eruption style plays a greater role than the volatile content of basalts in determining volcanic SO_2.

6 Discussion and Conclusion

The thermodynamic framework presented in this study provides a quantitative link between observations of volcanic deformation and degassing. The framework is used to explore the sensitivity of magma properties to several controlling parameters (magmatic H_2O, magmatic CO_2, magmatic S, oxygen fugacity f_{O_2}, crustal shear modulus μ, and chamber geometry), which vary systematically between tectonic setting. We demonstrated

that the results from thermodynamic models can be used to to calculate three key observables, SO_2 emissions, co-eruptive volume change and maximum vertical displacement, all of which are normalised by the erupted volume, and the dependence of these observables on pre-eruptive magmatic and chamber conditions. The conclusions of this study are as follow:

1. Magmas with high magmatic H_2O content have high SO_2 gas emissions and a high magma compressibility, which results in muted surface deformation during eruptions. While high magmatic CO_2 has little effect on SO_2 gas emissions, it increases magma compressibility and thus reduces surface deformation. Varying oxygen fugacity from NNO−1 to NNO+1 and increasing magmatic S increase sulfur gas emissions but has little effect magma compressibility.
2. Volcanoes with volatile-rich magma but stiff host rock have high magma compressibility and low chamber compressibility, respectively, which leads to more muted ground deformation during eruptions when compared to volcanoes that have volatile-poor magma and compliant host rock.
3. The volatile content of magmas varies between tectonic settings and this influences both ground deformation and degassing during eruptions. Arc basalts, which tend to have higher magmatic volatile contents, have more muted ground deformation than ocean island basalts, which is reflected in observations over the satellite era.

Our thermodynamic framework has the potential to link observations of volcanic deformation and degassing. However, there are caveats to this framework, such as 1) magma chambers with different geometries exhibit different magnitude of deformation (e.g., Gudmundsson, 2008; Amoruso & Crescentini, 2009; Anderson & Segall, 2011), 2) the magnitude of deformation may be influenced by viscoelastic responses of the crust (e.g., Hickey et al., 2013; Head et al., 2019; Gottsmann et al., 2020), 3) both magma composition and pre- and co-eruption gas segregation affect observations of deformation and degassing (e.g., Wallace, 2005; Edmonds et al., 2014; Edmonds & Woods, 2018), and 4) it is difficult to differentiate which parameter has the biggest influence on the observations of each eruption. Additional complexities listed above are not introduced to this framework as the goal of this study is to reconcile observations of volcanic deformation and degassing.

While the simplicity of this model is useful for considering general trends, oversimplification reduces the applicability to individual eruptions. The assumption of a typ-

ical crustal shear modulus may be appropriate for the sensitivity tests, but it is not applicable to all volcanoes. Similarly, we did not consider the effects of pre-eruptive gas segregation on magma properties, which in reality could affect co-eruptive observations (e.g., Wallace, 2001; Huppert & Woods, 2002; Rivalta & Segall, 2008). In practice, more parameters are needed to be considered to provide realism (Masterlark, 2003).

With results from the thermodynamic framework, we have developed a better understanding of the effects of magmatic volatile content and crustal compressibility on the physicochemical properties of magma. Our future work will explore pre-eruptive gas segregation processes such as gas accumulation and degassing to understand its implications on observations of volcanic deformation and degassing. Future studies should refine this framework for specific circumstances to resolve additional complexities.

Acknowledgments

This research is supported by the NERC-BGS Centre for the Observation and Modelling of Earthquakes Volcanoes and Tectonics (COMET) for SY, JB and ME. SY and JB are funded by the Leverhulme Trust, and PL acknowledges funding from the Embiricos Trust Scholarship from Jesus College, Cambridge.

References

Albino, F., Biggs, J., & Syahbana, D. K. (2019, 12). Dyke intrusion between neighbouring arc volcanoes re- sponsible for 2017 pre-eruptive seismic swarm at Agung, Bali. *Nature Communications*, *10*(1), 748. Retrieved from `http://www.nature.com/articles/s41467-019-08564-9http://dx.doi.org/10.1038/s41467-019-08564-9` doi: 10.1038/s41467-019-08564-9

Amoruso, A., & Crescentini, L. (2009, 2). Shape and volume change of pressurized ellipsoidal cavities from deformation and seismic data. *Journal of Geophysical Research*, *114*(B2), B02210. Retrieved from `http://doi.wiley.com/10.1029/2008JB005946` doi: 10.1029/2008JB005946

Anderson, K., & Segall, P. (2011, 7). Physics-based models of ground deformation and extrusion rate at effusively erupting volcanoes. *Journal of Geophysical Research: Solid Earth*, *116*(7), 1–20. Retrieved from `http://doi.wiley.com/10.1029/2010JB007939` doi: 10.1029/2010JB007939

Bachmann, O., & Bergantz, G. W. (2006, 1). Gas percolation in upper-crustal silicic

crystal mushes as a mechanism for upward heat advection and rejuvenation of near-solidus magma bodies. *Journal of Volcanology and Geothermal Research*, *149*(1-2), 85–102. doi: 10.1016/J.JVOLGEORES.2005.06.002

Belousov, A., Belousova, M., Edwards, B., Volynets, A., & Melnikov, D. (2015, 12). Overview of the precursors and dynamics of the 2012-13 basaltic fissure eruption of Tolbachik Volcano, Kamchatka, Russia. *Journal of Volcanology and Geothermal Research*, *307*, 22–37. doi: 10.1016/j.jvolgeores.2015.06.013

Biggs, J., Ebmeier, S. K., Aspinall, W. P., Lu, Z., Pritchard, M. E., Sparks, R. S., & Mather, T. A. (2014). Global link between deformation and volcanic eruption quantified by satellite imagery. *Nature Communications*, *5*. doi: 10.1038/ncomms4471

Biggs, J., & Pritchard, M. E. (2017). Global volcano monitoring: What does it mean when volcanoes deform? *Elements*, *13*(1), 17–22. doi: 10.2113/gselements.13.1.17

Biggs, J., & Wright, T. J. (2020, 12). *How satellite InSAR has grown from opportunistic science to routine monitoring over the last decade* (Vol. 11) (No. 1). Nature Research. Retrieved from `https://doi.org/10.1038/s41467-020-17587-6` doi: 10.1038/s41467-020-17587-6

Burgisser, A., Alletti, M., & Scaillet, B. (2015). Simulating the behavior of volatiles belonging to the C-O-H-S system in silicate melts under magmatic conditions with the software D-Compress. *Computers and Geosciences*. doi: 10.1016/j.cageo.2015.03.002

Burgisser, A., Chevalier, L., Gardner, J. E., & Castro, J. M. (2017, 7). The percolation threshold and permeability evolution of ascending magmas. *Earth and Planetary Science Letters*, *470*, 37–47. Retrieved from `http://dx.doi.org/10.1016/j.epsl.2017.04.023` doi: 10.1016/j.epsl.2017.04.023

Candela, P. A. (1997, 12). A Review of Shallow, Ore-related Granites: Textures, Volatiles, and Ore Metals. *Journal of Petrology*, *38*(12), 1619–1633. Retrieved from `https://academic.oup.com/petrology/article/38/12/1619/1604064` doi: 10.1093/PETROJ/38.12.1619

Carboni, E., Grainger, R. G., Mather, T. A., Pyle, D. M., Thomas, G. E., Siddans, R., ... Balis, D. (2016, 4). The vertical distribution of volcanic SO2 plumes measured by IASI. *Atmospheric Chemistry and Physics*, *16*(7), 4343–4367.

doi: 10.5194/acp-16-4343-2016

Carmichael, I. S., & Ghiorso, M. S. (1986, 6). Oxidation-reduction relations in basic magma: a case for homogeneous equilibria. *Earth and Planetary Science Letters*, *78*(2-3), 200–210. doi: 10.1016/0012-821X(86)90061-0

Carn, S. A., Clarisse, L., & Prata, A. J. (2016, 2). *Multi-decadal satellite measurements of global volcanic degassing* (Vol. 311). Elsevier B.V. doi: 10.1016/j.jvolgeores.2016.01.002

Carn, S. A., Fioletov, V. E., Mclinden, C. A., Li, C., & Krotkov, N. A. (2017, 3). A decade of global volcanic SO2 emissions measured from space. *Scientific Reports*, *7*(1), 1–12. Retrieved from `https://www.nature.com/articles/srep44095` doi: 10.1038/srep44095

Chaussard, E., & Amelung, F. (2014, 4). Regional controls on magma ascent and storage in volcanic arcs. *Geochemistry, Geophysics, Geosystems*, *15*(4), 1407–1418. Retrieved from `http://doi.wiley.com/10.1002/2013GC005216` doi: 10.1002/2013GC005216

Chaussard, E., Amelung, F., & Aoki, Y. (2013). Characterization of open and closed volcanic systems in Indonesia and Mexico using InSAR time series. *Journal of Geophysical Research: Solid Earth*. doi: 10.1002/jgrb.50288

Collins, S. J., Pyle, D. M., & Maclennan, J. (2009, 6). Melt inclusions track pre-eruption storage and dehydration of magmas at Etna. *Geology*, *37*(6), 571–574. doi: 10.1130/G30040A.1

Colombier, M., Wadsworth, F. B., Scheu, B., Vasseur, J., Dobson, K. J., Cáceres, F., ... Dingwell, D. B. (2020, 4). In situ observation of the percolation threshold in multiphase magma analogues. *Bulletin of Volcanology*, *82*(4), 1–15. Retrieved from `https://doi.org/10.1007/s00445-020-1370-1` doi: 10.1007/s00445-020-1370-1

Coppola, D., Laiolo, M., Cigolini, C., Massimetti, F., Delle Donne, D., Ripepe, M., ... William, R. (2020, 1). Thermal Remote Sensing for Global Volcano Monitoring: Experiences From the MIROVA System. *Frontiers in Earth Science*, *7*, 362. doi: 10.3389/FEART.2019.00362/BIBTEX

Delgado, F., Pritchard, M. E., Ebmeier, S., González, P., & Lara, L. (2017, 9). Recent unrest (2002–2015) imaged by space geodesy at the highest risk Chilean volcanoes: Villarrica, Llaima, and Calbuco (Southern An-

738 des). *Journal of Volcanology and Geothermal Research*, *344*, 270–288. doi:
739 10.1016/j.jvolgeores.2017.05.020

740 Duan, X. (2014). A general model for predicting the solubility behavior of
741 H2O-CO2 fluids in silicate melts over a wide range of pressure, tempera-
742 ture and compositions. *Geochimica et Cosmochimica Acta*, *125*, 582–609.
743 Retrieved from `http://dx.doi.org/10.1016/j.gca.2013.10.018` doi:
744 10.1016/j.gca.2013.10.018

745 Ebmeier, S. K., Andrews, B. J., Araya, M. C., Arnold, D. W. D., Biggs, J., Cooper,
746 C., ... Williamson, J. L. (2018, 12). Synthesis of global satellite observations
747 of magmatic and volcanic deformation: implications for volcano monitoring &
748 the lateral extent of magmatic domains. *Journal of Applied Volcanology*, *7*(1),
749 1–26. Retrieved from `https://appliedvolc.springeropen.com/articles/`
750 `10.1186/s13617-018-0071-3https://appliedvolc.biomedcentral.com/`
751 `track/pdf/10.1186/s13617-018-0071-3` doi: 10.1186/s13617-018-0071-3

752 Ebmeier, S. K., Biggs, J., Mather, T. A., & Amelung, F. (2013a). Applicability of
753 InSAR to tropical volcanoes: insights from Central America. *Geological Soci-*
754 *ety, London, Special Publications*. doi: 10.1144/SP380.2

755 Ebmeier, S. K., Biggs, J., Mather, T. A., & Amelung, F. (2013b, 5). *On the*
756 *lack of InSAR observations of magmatic deformation at Central Ameri-*
757 *can volcanoes* (Vol. 118) (No. 5). Blackwell Publishing Ltd. Retrieved
758 from `https://agupubs.onlinelibrary.wiley.com/doi/full/10.1002/`
759 `jgrb.50195https://agupubs.onlinelibrary.wiley.com/doi/abs/10.1002/`
760 `jgrb.50195https://agupubs.onlinelibrary.wiley.com/doi/10.1002/`
761 `jgrb.50195` doi: 10.1002/jgrb.50195

762 Ebmeier, S. K., Elliott, J. R., Nocquet, J. M., Biggs, J., Mothes, P., Jarrín, P.,
763 ... Samsonov, S. V. (2016, 9). Shallow earthquake inhibits unrest near
764 Chiles–Cerro Negro volcanoes, Ecuador–Colombian border. *Earth and Plane-*
765 *tary Science Letters*, *450*, 283–291. doi: 10.1016/j.epsl.2016.06.046

766 Edmonds, M., Cashman, K. V., Holness, M., & Jackson, M. (2019). Architecture
767 and dynamics of magma reservoirs. *Philosophical Transactions of the Royal So-*
768 *ciety A: Mathematical, Physical and Engineering Sciences*, *377*(2139). doi: 10
769 .1098/rsta.2018.0298

770 Edmonds, M., Humphreys, M. C., Hauri, E. H., Herd, R. A., Wadge, G., Rawson,

H., ... Guida, R. (2014, 1). Pre-eruptive vapour and its role in controlling eruption style and longevity at Soufrière Hills Volcano. *Geological Society Memoir*, *39*(1), 291–315. doi: 10.1144/M39.16

Edmonds, M., Mather, T. A., & Liu, E. J. (2018). A distinct metal fingerprint in arc volcanic emissions. *Nature Geoscience*, *11*(10), 790–794. Retrieved from http://dx.doi.org/10.1038/s41561-018-0214-5 doi: 10.1038/s41561-018-0214-5

Edmonds, M., & Woods, A. W. (2018). Exsolved volatiles in magma reservoirs. *Journal of Volcanology and Geothermal Research*, *368*, 13–30. Retrieved from https://doi.org/10.1016/j.jvolgeores.2018.10.018 doi: 10.1016/j.jvolgeores.2018.10.018

Fialko, Y., Simons, M., & Agnew, D. (2001, 8). The complete (3-D) surface displacement field in the epicentral area of the 1999 Mw 7.1 Hector Mine earthquake, California, from space geodetic observations. *Geophysical Research Letters*, *28*(16), 3063–3066. Retrieved from https://agupubs.onlinelibrary.wiley.com/doi/full/10.1029/2001GL013174https://agupubs.onlinelibrary.wiley.com/doi/abs/10.1029/2001GL013174https://agupubs.onlinelibrary.wiley.com/doi/10.1029/2001GL013174 doi: 10.1029/2001GL013174

Furtney, M. A., Pritchard, M. E., Biggs, J., Carn, S. A., Ebmeier, S. K., Jay, J. A., ... Reath, K. A. (2018, 10). Synthesizing multi-sensor, multi-satellite, multi-decadal datasets for global volcano monitoring. *Journal of Volcanology and Geothermal Research*, *365*, 38–56. doi: 10.1016/j.jvolgeores.2018.10.002

Gaillard, F., & Scaillet, B. (2014, 10). A theoretical framework for volcanic degassing chemistry in a comparative planetology perspective and implications for planetary atmospheres. *Earth and Planetary Science Letters*, *403*, 307–316. doi: 10.1016/j.epsl.2014.07.009

Ge, C., Wang, J., Carn, S., Yang, K., Ginoux, P., & Krotkov, N. (2016, 4). Satellite-based global volcanic SO2 emissions and sulfate direct radiative forcing during 2005-2012. *Journal of Geophysical Research*, *121*(7), 3446–3464. Retrieved from https://agupubs.onlinelibrary.wiley.com/doi/full/10.1002/2015JD023134https://agupubs.onlinelibrary.wiley.com/doi/abs/10.1002/2015JD023134https://agupubs.onlinelibrary.wiley.com/doi/

804 10.1002/2015JD023134 doi: 10.1002/2015JD023134

805 Girona, T., Costa, F., Newhall, C., & Taisne, B. (2014, 12). On depressurization
806 of volcanic magma reservoirs by passive degassing. *Journal of Geophysical Re-*
807 *search: Solid Earth*, *119*(12), 8667–8687. Retrieved from http://doi.wiley
808 .com/10.1002/2014JB011368 doi: 10.1002/2014JB011368

809 Gottsmann, J., Biggs, J., Lloyd, R., Biranhu, Y., & Lewi, E. (2020, 4). Ductility and
810 compressibility accommodate high magma flux beneath a silicic continental rift
811 caldera: Insights from Corbetti caldera (Ethiopia). *Geochemistry, Geophysics,*
812 *Geosystems*, *21*(4), e2020GC008952. doi: 10.1029/2020gc008952

813 Gualda, G. A., Ghiorso, M. S., Lemons, R. V., & Carley, T. L. (2012, 5). Rhyolite-
814 MELTS: a Modified Calibration of MELTS Optimized for Silica-rich, Fluid-
815 bearing Magmatic Systems. *Journal of Petrology*, *53*(5), 875–890. Retrieved
816 from https://academic.oup.com/petrology/article/53/5/875/1527627
817 doi: 10.1093/PETROLOGY/EGR080

818 Gudmundsson, A. (2005, 9). The effects of layering and local stresses in composite
819 volcanoes on dyke emplacement and volcanic hazards. *Comptes Rendus - Geo-*
820 *science*, *337*(13), 1216–1222. doi: 10.1016/j.crte.2005.07.001

821 Gudmundsson, A. (2008, 1). *Chapter 8 Magma-Chamber Geometry, Fluid Trans-*
822 *port, Local Stresses and Rock Behaviour During Collapse Caldera Formation*
823 (Vol. 10) (No. C). Elsevier. doi: 10.1016/S1871-644X(07)00008-3

824 Hamling, I. J., Cevuard, S., & Garaebiti, E. (2019, 5). Large-Scale Drainage of a
825 Complex Magmatic System: Observations From the 2018 Eruption of Am-
826 brym Volcano, Vanuatu. *Geophysical Research Letters*, *46*(9), 4609–4617. doi:
827 10.1029/2019GL082606

828 Hautmann, S., Gottsmann, J., Sparks, R. S. J., Mattioli, G. S., Sacks, I. S., &
829 Strutt, M. H. (2010, 9). Effect of mechanical heterogeneity in arc crust on
830 volcano deformation with application to Soufrière Hills Volcano, Montserrat,
831 West Indies. *Journal of Geophysical Research: Solid Earth*, *115*(B9), 9203.
832 Retrieved from https://onlinelibrary.wiley.com/doi/full/10.1029/
833 2009JB006909https://onlinelibrary.wiley.com/doi/abs/10.1029/
834 2009JB006909https://agupubs.onlinelibrary.wiley.com/doi/10.1029/
835 2009JB006909 doi: 10.1029/2009JB006909

836 Head, M., Hickey, J., Gottsmann, J., & Fournier, N. (2019, 8). The Influ-

ence of Viscoelastic Crustal Rheologies on Volcanic Ground Deformation: Insights From Models of Pressure and Volume Change. *Journal of Geophysical Research: Solid Earth*, *124*(8), 8127–8146. Retrieved from https://onlinelibrary.wiley.com/doi/10.1029/2019JB017832 doi: 10.1029/2019JB017832

Heap, M. J., Villeneuve, M., Albino, F., Farquharson, J. I., Brothelande, E., Amelung, F., ... Baud, P. (2020, 1). Towards more realistic values of elastic moduli for volcano modelling. *Journal of Volcanology and Geothermal Research*, *390*, 106684. doi: 10.1016/j.jvolgeores.2019.106684

Hickey, J., Gottsmann, J., & Del Potro, R. (2013, 3). The large-scale surface uplift in the Altiplano-Puna region of Bolivia: A parametric study of source characteristics and crustal rheology using finite element analysis. *Geochemistry, Geophysics, Geosystems*, *14*(3), 540–555. Retrieved from https://agupubs.onlinelibrary.wiley.com/doi/full/10.1002/ggge.20057https://agupubs.onlinelibrary.wiley.com/doi/abs/10.1002/ggge.20057https://agupubs.onlinelibrary.wiley.com/doi/10.1002/ggge.20057 doi: 10.1002/ggge.20057

Huppert, H. E., & Woods, A. W. (2002). The role of volatiles in magma chamber dynamics. *Nature*, *420*(6915), 493–495. doi: 10.1038/nature01211

Kilbride, B. M. C., Edmonds, M., & Biggs, J. (2016, 12). Observing eruptions of gas-rich compressible magmas from space. *Nature Communications*, *7*(1), 1–8. Retrieved from http://dx.doi.org/10.1038/ncomms13744www.nature.com/naturecommunications doi: 10.1038/ncomms13744

Liggins, P., Jordan, S., Rimmer, P. B., & Shorttle, O. (2021, 11). Growth and evolution of secondary volcanic atmospheres: I. Identifying the geological character of warm rocky planets. *arXiv*. Retrieved from https://arxiv.org/abs/2111.05161v1

Liggins, P., Shorttle, O., & Rimmer, P. B. (2020, 11). Can volcanism build hydrogen-rich early atmospheres? *Earth and Planetary Science Letters*, *550*, 116546. doi: 10.1016/J.EPSL.2020.116546

Lindoo, A., Larsen, J. F., Cashman, K. V., & Oppenheimer, J. (2017, 9). Crystal controls on permeability development and degassing in basaltic andesite magma. *Geology*, *45*(9), 831–834. Retrieved from https://imagej.nih.gov

870 doi: 10.1130/G39157.1

871 Lowenstern, J. B. (1994, 10). Dissolved volatile concentrations in an ore-forming
872 magma. *Geology*, *22*(10), 893–896. doi: 10.1130/0091-7613(1994)022⟨0893:
873 dvciao⟩2.3.co;2

874 Masterlark, T. (2003, 11). Finite element model predictions of static deforma-
875 tion from dislocation sources in a subduction zone: Sensitivities to homo-
876 geneous, isotropic, Poisson-solid, and half-space assumptions. *Journal of*
877 *Geophysical Research: Solid Earth*, *108*(B11), 2540. Retrieved from `https://`
878 `onlinelibrary.wiley.com/doi/full/10.1029/2002JB002296https://`
879 `onlinelibrary.wiley.com/doi/abs/10.1029/2002JB002296https://`
880 `agupubs.onlinelibrary.wiley.com/doi/10.1029/2002JB002296` doi:
881 10.1029/2002JB002296

882 Mogi, K. (1958). Relations between the eruptions of various volcanoes and the
883 deformations of the ground surfaces around them. *Bulletin of the Earthquake*
884 *Research Institute*, *36*, 99–134. Retrieved from `http://repository.dl.itc`
885 `.u-tokyo.ac.jp/dspace/handle/2261/11909%5Cnpapers://8461d6ef-4184`
886 `-45b2-aa3d-395291ea6525/Paper/p3868` doi: 10.1016/j.epsl.2004.04.016

887 Morales Rivera, A. M., Amelung, F., & Mothes, P. (2016, 7). Volcano deforma-
888 tion survey over the Northern and Central Andes with ALOS InSAR time
889 series. *Geochemistry, Geophysics, Geosystems*, *17*(7), 2869–2883. Re-
890 trieved from `https://onlinelibrary.wiley.com/doi/full/10.1002/`
891 `2016GC006393https://onlinelibrary.wiley.com/doi/abs/10.1002/`
892 `2016GC006393https://agupubs.onlinelibrary.wiley.com/doi/10.1002/`
893 `2016GC006393` doi: 10.1002/2016GC006393

894 Moran, S. C., Kwoun, O., Masterlark, T., & Lu, Z. (2006, 2). On the absence of
895 InSAR-detected volcano deformation spanning the 1995–1996 and 1999 erup-
896 tions of Shishaldin Volcano, Alaska. *Journal of Volcanology and Geothermal*
897 *Research*, *150*(1-3), 119–131. doi: 10.1016/J.JVOLGEORES.2005.07.013

898 Naismith, A. K., Matthew Watson, I., Escobar-Wolf, R., Chigna, G., Thomas, H.,
899 Coppola, D., & Chun, C. (2019, 2). Eruption frequency patterns through time
900 for the current (1999–2018) activity cycle at Volcán de Fuego derived from
901 remote sensing data: Evidence for an accelerating cycle of explosive paroxysms
902 and potential implications of eruptive activity. *Journal of Volcanology and*

Geothermal Research, *371*, 206–219. doi: 10.1016/j.jvolgeores.2019.01.001

Neal, C. A., Brantley, S. R., Antolik, L., Babb, J. L., & Etc. (2019). The 2018 rift eruption and summit collapse of Kīlauea Volcano. *Science*, *363*(January), 367–374.

Ohmoto, H., & Kerrick, D. M. (1977, 10). Devolatilization equilibria in graphitic systems. *American Journal of Science*, *277*(8), 1013–1044. Retrieved from http://www.ajsonline.org/content/277/8/1013 doi: 10.2475/ajs.277.8.1013

Okada, Y. (1985). *SURFACE DEFORMATION DUE TO SHEAR AND TENSILE FAULTS IN A HALF-SPACE* (Vol. 75; Tech. Rep. No. 4). Retrieved from http://www.bosai.go.jp/study/application/dc3d/download/Okada_1985_BSSA.pdf

Papale, P. (1999). Modeling of the solubility of a two-component H2O + CO2 fluid in silicate liquids. *American Mineralogist*, *84*(4), 477–492. doi: 10.2138/am-1999-0402

Papale, P., Moretti, R., & Barbato, D. (2006). The compositional dependence of the saturation surface of H 2O + CO 2 fluids in silicate melts. *Chemical Geology*, *229*(1-3), 78–95. doi: 10.1016/j.chemgeo.2006.01.013

Piochi, M., Bruno, P. P., De Astis, G., Piochi, M., Bruno, P. P., & De Astis, G. (2005, 7). Relative roles of rifting tectonics and magma ascent processes: Inferences from geophysical, structural, volcanological, and geochemical data for the Neapolitan volcanic region (southern Italy). *Geochemistry, Geophysics, Geosystems*, *6*(7). Retrieved from https://onlinelibrary.wiley.com/doi/full/10.1029/2004GC000885https://onlinelibrary.wiley.com/doi/abs/10.1029/2004GC000885https://agupubs.onlinelibrary.wiley.com/doi/10.1029/2004GC000885 doi: 10.1029/2004GC000885

Plank, T., Kelley, K. A., Zimmer, M. M., Hauri, E. H., & Wallace, P. J. (2013, 2). Why do mafic arc magmas contain ˜4wt% water on average? *Earth and Planetary Science Letters*, *364*, 168–179. doi: 10.1016/j.epsl.2012.11.044

Prata, A. J., & Kerkmann, J. (2007, 3). Simultaneous retrieval of volcanic ash and SO2 using MSG-SEVIRI measurements. *Geophysical Research Letters*, *34*(5). Retrieved from https://agupubs.onlinelibrary.wiley.com/doi/full/10.1029/2006GL028691https://agupubs.onlinelibrary.wiley.com/doi/

abs/10.1029/2006GL028691https://agupubs.onlinelibrary.wiley.com/doi/10.1029/2006GL028691 doi: 10.1029/2006GL028691

Pritchard, M. E., Biggs, J., Wauthier, C., Sansosti, E., Arnold, D. W., Delgado, F., ... Zoffoli, S. (2018). Towards coordinated regional multi-satellite InSAR volcano observations: results from the Latin America pilot project. *Journal of Applied Volcanology*, *7*(1). doi: 10.1186/s13617-018-0074-0

Reath, K., Pritchard, M., Biggs, J., Andrews, B., Ebmeier, S. K., Bagnardi, M., ... Poland, M. (2020, 1). Using Conceptual Models to Relate Multiparameter Satellite Data to Subsurface Volcanic Processes in Latin America. *Geochemistry, Geophysics, Geosystems*, *21*(1), 1–26. doi: 10.1029/2019GC008494

Reath, K., Pritchard, M., Poland, M., Delgado, F., Carn, S., Coppola, D., ... Bagnardi, M. (2019, 1). Thermal, Deformation, and Degassing Remote Sensing Time Series (CE 2000–2017) at the 47 most Active Volcanoes in Latin America: Implications for Volcanic Systems. *Journal of Geophysical Research: Solid Earth*, *124*(1), 195–218. Retrieved from https://onlinelibrary.wiley.com/doi/abs/10.1029/2018JB016199http://doi.wiley.com/10.1029/2018JB016199 doi: 10.1029/2018JB016199

Rivalta, E., & Segall, P. (2008). Magma compressibility and the missing source for some dike intrusions. *Geophysical Research Letters*, *35*(4), 1–5. doi: 10.1029/2007GL032521

Rust, A. C., & Cashman, K. V. (2011, 11). Permeability controls on expansion and size distributions of pyroclasts. *Journal of Geophysical Research: Solid Earth*, *116*(11). Retrieved from https://agupubs.onlinelibrary.wiley.com/doi/full/10.1029/2011JB008494https://agupubs.onlinelibrary.wiley.com/doi/abs/10.1029/2011JB008494https://agupubs.onlinelibrary.wiley.com/doi/10.1029/2011JB008494 doi: 10.1029/2011JB008494

Scaillet, B., & Pichavant, M. (2005). A model of sulphur solubility for hydrous mafic melts: application to the determination of magmatic fluid compositions of Italian volcanoes. *Annals of Geophysics*. Retrieved from https://www.earth-prints.org/handle/2122/930

Sigmundsson, F., Pinel, V., Grapenthin, R., Hooper, A., Halldórsson, S. A., Einarsson, P., ... Yamasaki, T. (2020, 12). Unexpected large eruptions from buoyant magma bodies within viscoelastic crust. *Nature Communications*, *11*(1), 1–

11. Retrieved from https://doi.org/10.1038/s41467-020-16054-6 doi: 10.1038/s41467-020-16054-6

Spera, F. J. (2000). Physical properties of magma. *Encyclopedia on Volcanoes*. Retrieved from https://ci.nii.ac.jp/naid/10015606430

Telling, J., Flower, V. J., & Carn, S. A. (2015, 12). A multi-sensor satellite assessment of SO2 emissions from the 2012–13 eruption of Plosky Tolbachik volcano, Kamchatka. *Journal of Volcanology and Geothermal Research*, *307*, 98–106. doi: 10.1016/J.JVOLGEORES.2015.07.010

Theys, N., Hedelt, P., De Smedt, I., Lerot, C., Yu, H., Vlietinck, J., ... Van Roozendael, M. (2019, 12). Global monitoring of volcanic SO 2 degassing with unprecedented resolution from TROPOMI onboard Sentinel-5 Precursor. *Scientific Reports*, *9*(1), 1–10. Retrieved from www.nature.com/scientificreports doi: 10.1038/s41598-019-39279-y

Voight, B., Widiwijayanti, C., Mattioli, G., Elsworth, D., Hidayat, D., & Strutt, M. (2010, 10). Magma-sponge hypothesis and stratovolcanoes: Case for a compressible reservoir and quasi-steady deep influx at Soufrière Hills Volcano, Montserrat. *Geophysical Research Letters*, *37*(19), n/a-n/a. Retrieved from http://doi.wiley.com/10.1029/2009GL041732 doi: 10.1029/2009GL041732

Wallace, P. J. (2001). Volcanic SO2 emissions and the abundance and distribution of exsolved gas in magma bodies. *Journal of Volcanology and Geothermal Research*, *108*(1-4), 85–106. doi: 10.1016/S0377-0273(00)00279-1

Wallace, P. J. (2005, 1). Volatiles in subduction zone magmas: Concentrations and fluxes based on melt inclusion and volcanic gas data. *Journal of Volcanology and Geothermal Research*, *140*(1-3), 217–240. doi: 10.1016/j.jvolgeores.2004.07.023

Wallace, P. J., & Carmichael, I. S. (1992, 5). Sulfur in basaltic magmas. *Geochimica et Cosmochimica Acta*, *56*(5), 1863–1874. doi: 10.1016/0016-7037(92)90316-B

Wallace, P. J., & Carmichael, I. S. (1999, 6). Quaternary volcanism near the Valley of Mexico: Implications for subduction zone magmatism and the effects of crustal thickness variations on primitive magma compositions. *Contributions to Mineralogy and Petrology*, *135*(4), 291–314. doi: 10.1007/s004100050513

Wallace, P. J., & Gerlach, T. M. (1994, 7). Magmatic vapor source for sulfur dioxide

released during volcanic eruptions: Evidence from Mount Pinatubo. *Science*, *265*(5171), 497–499. Retrieved from http://science.sciencemag.org/ doi: 10.1126/science.265.5171.497

Wong, Y., & Segall, P. (2020, 11). Joint Inversions of Ground Deformation, Extrusion Flux, and Gas Emissions Using Physics-Based Models for the Mount St. Helens 2004–2008 Eruption. *Geochemistry, Geophysics, Geosystems*, *21*(12), 1–24. Retrieved from https://agupubs.onlinelibrary.wiley.com/doi/full/10.1029/2020GC009343https://agupubs.onlinelibrary.wiley.com/doi/abs/10.1029/2020GC009343https://agupubs.onlinelibrary.wiley.com/doi/10.1029/2020GC009343 doi: 10.1029/2020GC009343

Wong, Y., Segall, P., Bradley, A., & Anderson, K. (2017). Constraining the Magmatic System at Mount St. Helens (2004–2008) Using Bayesian Inversion With Physics-Based Models Including Gas Escape and Crystallization. *Journal of Geophysical Research: Solid Earth*, *122*(10), 7789–7812. doi: 10.1002/2017JB014343

Woods, A. W., & Huppert, H. E. (2003). On magma chamber evolution during slow effusive eruptions. *Journal of Geophysical Research*, *108*(B8), 1–16. doi: 10.1029/2002jb002019

Yang, X.-M., Davis, P. M., & Dieterich, J. H. (1988, 5). Deformation from inflation of a dipping finite prolate spheroid in an elastic half-space as a model for volcanic stressing. *Journal of Geophysical Research: Solid Earth*, *93*(B5), 4249–4257. Retrieved from http://doi.wiley.com/10.1029/JB093iB05p04249 doi: 10.1029/JB093iB05p04249

Yip, S. T. H., Biggs, J., & Albino, F. (2019, 12). Reevaluating Volcanic Deformation Using Atmospheric Corrections: Implications for the Magmatic System of Agung Volcano, Indonesia. *Geophysical Research Letters*, *46*(23), 13704–13711. Retrieved from https://onlinelibrary.wiley.com/doi/full/10.1029/2019GL085233https://onlinelibrary.wiley.com/doi/abs/10.1029/2019GL085233https://agupubs.onlinelibrary.wiley.com/doi/10.1029/2019GL085233 doi: 10.1029/2019GL085233

Zhan, Y., Gregg, P. M., Le Mével, H., Miller, C. A., & Cardona, C. (2019, 12). Integrating Reservoir Dynamics, Crustal Stress, and Geophysical Observations of the Laguna del Maule Magmatic System by FEM Models and Data Assim-

ilation. *Journal of Geophysical Research: Solid Earth*, *124*(12), 13547–13562. Retrieved from https://onlinelibrary.wiley.com/doi/abs/10.1029/2019JB018681 doi: 10.1029/2019JB018681

Zimmer, M. M., Plank, T., Hauri, E. H., Yogodzinski, G. M., Stelling, P., Larsen, J., ... Nye, C. J. (2010, 12). The role of water in generating the calc-alkaline trend: New volatile data for aleutian magmas and a new tholeiitic index. *Journal of Petrology*, *51*(12), 2411–2444. Retrieved from https://academic.oup.com/petrology/article/51/12/2411/1541257 doi: 10.1093/petrology/egq062